Department of Physics and Astronomy
Heidelberg University

Bachelor Thesis in Physics
submitted by

Nils Anthon

born in Gerolstein (Germany)

2026

Evaluation of Focused Beam-Assisted Carbon Deposition as a Post-Fabrication Trimming Technique for Lithium Niobate Photonic Devices

This Bachelor Thesis has been carried out by Nils Anthon at the
Kirchhoff-Institut für Physik of the Ruprecht-Karls-University of Heidelberg
under the supervision of
Prof. Dr. Wolfram Pernice

Abstract

This thesis investigates whether carbon deposition is a viable post-fabrication trimming method for lithium niobate on insulator (LNOI). LNOI photonic devices are highly sensitive to fabrication imperfections, so controlled trimming methods are needed to adjust optical properties without causing damages. Focused ion beam (FIB) and electron beam (EBeam) assisted carbon deposition were evaluated on racetrack resonators to determine viability for LNOI. The resonance spectra, quality factors, effective refractive indices and propagation loss of the devices were measured before and after trimming. FIB deposition caused strong degradation of resonator performance, with significant reductions in Q-factor and large increases in propagation loss, while EBeam deposition produced much less damage and measurable resonance shifts with less losses. Improved technique with lowered acceleration voltage of the EBeam, increased probe current and additional, untrimmed reference resonators was tested to distinguish trimming changes and environmental or instrumental changes. The results show that EBeam assisted carbon deposition is the more promising trimming strategy for LNOI waveguides and provide a first experimental foundation for post-fabrication trimming of lithium niobate photonic circuits.

Zusammenfassung

Diese Arbeit untersucht, ob Kohlenstoffablagerung als nachträgliche Trimmtechnik für Lithiumniobat-auf-Isolator (LNOI) Wellenleiter realisierbar ist. Aufgrund der Empfindlichkeit von LNOI werden kontrollierte Trimmverfahen benötigt, um optische Eigenschaften anzupassen, ohne die Plattform zu beschädigen. Es wurden die durch FIB und EBeam unterstütze Kohlenstoffablagerung an Racetrack-Resonatoren untersucht, um ihre Eignung für LNOI zu bestimmen. Die Resonanzspektren, Gütefaktoren, effektiven Brechungsindizes und Verluste der Bauelemente wurden vor und nach dem Trimmen gemessen. Die FIB Methode verursachte eine starke Verschlechterung, mit deutlichen Reduktionen des Gütefaktors und großen Erhöhungen der Verluste, während die EBeam Methode wesentlich geringere Schäden verursachte und messbare Resonanzverschiebungen bei geringen Verlusten ermöglichte. Die Technik wurde verbessert mit verringerter Beschleunigungsspannung des EBeam, erhöhtem Sondenstroms und der Einführung zusätzlicher, ungetrimmter Referenzresonatoren, um Trimmveränderungen von umgebungs- und instrumentenbedingte Änderungen unterscheiden zu können. Die Ergebnisse zeigen, dass Elektronenstrahl unterstützte Kohlenstoffablagerung die vielversprechendere Trimmstrategie for LNOI-Wellenleiter ist und liefern eine erste experimentelle Grundlage für das nachträgliche Trimmen von photonischen Schaltungen aus Lithiumniobat.

Contents

1 Introduction **3**

2 Theoretical background **4**

2.1 Material properties of bulk LN 4

2.2 Thin-film lithium niobate and LNOI 7

2.3 LN Waveguides and fabrication methods 8

2.3.1 Ridge/rib waveguides on LNOI 11

2.3.2 Fabrication of fully etched LNOI waveguides 12

2.4 Guided modes 13

2.5 Important understanding for racetracks 14

3 Experimental methods and setup **16**

3.1 Photonic devices and laboratory setup 16

3.2 FIB assisted carbon deposition 20

3.3 EBeam assisted carbon deposition 22

3.4 Evaluation procedure 24

3.5 Used trimming recipes 25

3.5.1 FIB 25

3.5.2 EBeam 26

4 Results **26**

4.1 Results for FIB recipes 26

4.2 Results for EBeam recipes 29

4.3 Improved experimental methodology 34

4.4 Comparison to results for LTOI 36

5 Conclusion **36**

5.1 Summary 37

5.2 Outlook 38

6 References **39**

6.1 Acknowledgement 39

1 Introduction

Photonic integrated circuits (PICs), used in optical communications and computing for low-cost and scaled solutions, bring together multiple photonic components with different functions on a single chip, that are highly sensitive towards fabrication imperfections. These imperfections will accumulate fast in such a system, leading to the need of precise post-fabrication trimming to compensate these imperfections. The most commonly used material platform for photonics is silicon nitride, but many other material systems have been investigated for integrated photonics. Many of those platforms struggle to simultaneously support ultra-low propagation loss, fast and low-loss optical modulation, and efficient all-optical nonlinearities.

A promising photonic platform for this is lithium niobate (LN), which, due to its great electro-, nonlinear-, and acousto-optic properties, wide transparency window and relatively high refractive index, excels in versatility [1]. At the same time, this versatility can also lead to more unpredictable and unstable behaviour compared to that of silicon nitride, further increasing the need for post-fabrication trimming.
With increasing demands for signal transmission capacity, the high power and large size of bulk LN-based devices pose great challenges, while integrated silicon photonics already experienced dramatic developments in recent decades [2]. More recently, LN on insulator (LNOI) became commercially available, which made LN photonics a very relevant research topic and many developments in LN photonics possible [2]. LNOI allows light to be more confined within a compact structure, because of its high refractive index contrast [2]. Together with before mentioned beneficial properties of LN, various kinds of high-performance integrated LN devices are possible, which makes LN-based photonic platforms and ways to influence or improve the functionality of devices on those platforms highly interesting research topics.

Although many fabrication induced imperfections can be reduced through improved fabrication processes, optimized designs or careful packaging, some deviations can not be fully eliminated. For these cases post-fabrication trimming techniques are required, which should provide controlled and stable tuning of the optical properties without introducing damage to the platform.

In 2025, a method using carbon deposition was successfully shown to be a scalable, robust, and low-loss method for precisely controlling the optical path lengths in silicon nitride photonic integrated circuit devices by the group in which this thesis was carried out [3]. The same method using Carbon deposition was used to tune Asymmetric Directional Couplers, which are used for on-chip mode conversion between selected modes. This requires phase matching by equalizing the modes effective refractive indices at a given

wavelength[4][3]. While carbon trimming has been demonstrated for SiN, its applicability to LNOI has not yet been investigated.

In this thesis, the applicability of the methods used for carbon deposition on silicon nitride photonic integrated circuit devices will be tested and evaluated for LN-based platforms to compensate for the post-fabrication imperfections. This work will serve to lay a first foundation for carbon deposition on LNOI waveguides and further investigations for the proposed techniques. It is aimed to answer the following questions:

1. How does FIB assisted and EBeam assisted carbon deposition influence Q-factor and propagation loss?
2. How do both techniques perform compared to each other?
3. How do different parameters in the trimming recipes affect optical response?
4. How stable are the induced changes?
5. What conditions have to be met for feasible carbon deposition?

For this, different deposition recipes for the proposed methods will be tested and evaluated on LNOI waveguides.

2 Theoretical background

This section will give a good foundation and understanding of the potential of LN in photonics. First the Material properties of bulk LN must be understood, explaining the attractiveness of LN-based photonic devices, and the fabrication of thin-film LN and LNOI ridge waveguides will be explained, to give a general understanding on where fabrication imperfections can occur, what could degrade waveguide quality and what general values for LNOI waveguides are for most commonly used fabrication techniques. Lastly, it is briefly explained why carbon deposition on top of a waveguide influences the optical response of a resonator and equations used for calculating important values for racetrack resonators are presented.

2.1 Material properties of bulk LN

LN has been an important material in photonics since its ferroelectric properties were first discovered and it has many superior characteristics compared to other materials used

in photonics, such as a wide transparency window of $400nm$ to $5\mu m$, large electro-optic (EO), nonlinear-optic (NLO), acousto-optic (AO) and pyroelectric coefficients and stable chemical and physical properties [2].
LN is not a naturally occurring material and was first grown by the Czochralski method in 1965 [5]. The crystal structure of LN exhibits three-fold rotation symmetry about the z-axis and mirror symmetry about three planes that are 60 degrees apart[1]. Consequently LN belongs to the 3m point group and the crystal structure rhombohedral and can be seen in figure 1 (a), showing the relative positions of lithium (Li) and nobium (Nb) with respect to the oxygen (O) octahedra. The oxygen atoms form a nearly hexagonal close-packed lattice, where the cations occupy the octahedral sites in a sequence of Nb-Li-vacancy-Nb-Li-vacancy [5]. This asymmetric distribution of the ions in the crystal structure leads to considerable spontaneous polarization even at room temperature [6]. Because of this, external forces can change the polarization, which causes inhomogeneity in charge distribution, resulting in the piezoelectric effect of LN [6]. The polarization direction is along the z-axis of the crystal, and the polarization intensity is 50 $\mu C/cm^2$ [6]. The ferroelectric domain orientation can be inverted using a strong external electric field, which can relocate Li and Nb with Li moving to the adjacent vacancy and Nb only moving slightly, as also shown in figure 1 (a) [1].

In LN's crystal structure, about one-third of octahedral sites contain Li, one-third Nb and one-third remain vacant. Stoichiometric LN is the idealized form of LN, where the Li/Nb ratio is equal to 1 with nearly ideal crystal structure [5]. It has a low defect density, which leads to better optical performance and higher resistance to laser damage [5]. More commonly used and most commercially grown is congruent LN with a Li/Nb ratio approximately equal to 0.946. For congruent Ln, Li deficiency causes Nb ions to occupy Li sites (also known as Nb antisite defects), which leads to a higher defect concentration [5]. This makes congruent LN more susceptible to laser-induced damage. Other common defects are more Vacancies, where ions are missing and impurity atoms.
Defects strongly determine LN's properties and even impurity levels of $\approx 0.01\%$ can significantly alter dielectric and optical properties and also the laser damage threshold [5].

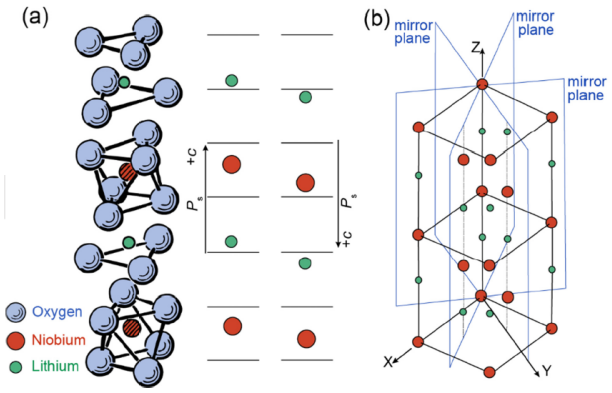


Figure 1: Crystal structure of lithium niobate. (a) Positions of lithium and niobium atoms with respect to oxygen octahedra in the ferroelectric phase. Poling moves the positions of Li and Nb, resulting in the inversion of the spontaneous polarization and domain orientation. (b) Standard definition of X, Y, and Z axes, where Y aligns with a mirror plane. Taken unchanged from [1]

The EO effect of LN is closely related to its ferroelectric properties and an applied electric field can affect the spontaneous polarization of the material. Due to the change in spontaneous polarization, a change in refractive index can be caused [6]. Adjusting the applied electric field can be utilised to use the EO effect of LN for an efficient optical modulation function [7].
The EO tensor of LN

$$r_{ij} = \begin{bmatrix} 0 & -r_{22} & r_{13} \\ 0 & r_{22} & r_{13} \\ 0 & 0 & r_{33} \\ 0 & r_{42} & 0 \\ r_{42} & 0 & 0 \\ r_{22} & 0 & 0 \end{bmatrix} \tag{1}$$

describes the responsiveness of refractive index relative to changes in the electric field. The EO effect can be divided into linear EO effect or Pockels effect and quadratic EO effect or Kerr effect [6]. Due to the LNs particularly prominent r_{33} EO coefficient of $\approx 30.9\, pm/V$, the response of the material to an electric field, and therefore the EO effect, is mainly linear [2].

With a transparency range of $0.35 - 5\mu m$, LN is optically transparent throughout the visible and much of the infrared spectrum and beyond $5\mu m$ lattice absorption becomes significant [5]. Wavelengths of around $1.3 - 1.55\mu m$ are being used in optical communications, which makes LN especially interesting for this range.
LN's wide optical bandgap with reported values ranging from 3.57 to $4.7eV$ contributes to its high transparency window [5]. The values for this bandgap can vary due to crystal defects and stoichiometry, which introduce localized electronic states and band-tail

absorption [5]. Defects can thus increase optical absorption and greatly reduce device performance.

LN is birefringent, meaning light experiences different refractive indices depending on its polarization and propagation direction [5]. At $1550nm$, bulk single-crystal LN is typically reported with an ordinary refractive index of $n_0 \approx 2.21$ and an extraordinary refractive index of $n_e \approx 2.14$, which can vary slightly with crystal composition, temperature and wether the material is congruent or stoichiometric [8]. This birefringence enables polarization control and is essential for phase matching in nonlinear optical processes like second-harmonic generation [9].

LNOI-based photonic devices today are predominantly from one of two types of TFLN slabs [10]. For so called "X-cut" LN devices, which are used in this thesis, the core layers are cut from bulk LN along planes that are perpendicular to one of its ordinary (x- or y-axis) axes [10]. "Z-cut" devices are consequently cut along the plane perpendicular to its extraordinary axis (z-axis) [10].

Due to LNs relatively large refractive index of 2.2 at $1550nm$, high-index-contrast waveguides can be formed on top of most amorphous and crystal substrates (e.g. SiO_2 or sapphire), which enables good light confinement [1].

2.2 Thin-film lithium niobate and LNOI

Thin-film lithium niobate (TFLN) most often refers to sub-micron to a few-micron single-crystal LN layers, that are bonded on a low-index insulator [9]. This high index contrast between the LN and the low-index insulator provides strong optical confinement and enables integrated photonics.
LNOI refers to the specific platform where a crystalline LN film is bonded to an insulator layer on a mechanically robust handle wafer or substrate [2].

Traditional bulk LN photonic devices suffered from low index contrast, large optical modes, high drive voltages, poor RF-optical matching and inability to form compact structures like tight bends or resonators [1]. These constraints also hinder large-scale integration on a single chip, so TFLN was developed to overcome these key limitations [1]. Many early attempts to fabricate TFLN using deposition and growth techniques failed to achieve high crystalline quality and were limited by substrate compatibility [1].

The method commonly used today for TFLN fabrication is the "Smart Cut" technique, which was adapted from silicon-on-insulator fabrication and was a major breakthrough in LNOI fabrication [1]. The schematic of this Smart Cut process for a LNOI wafer can

be seen in figure 2. This method does not grow the film on the substrate directly, but it slices a thin layer from a high-quality bulk LN crystal using ion implantation and thermal annealing, after which it is bonded to an insulating substrate [1].

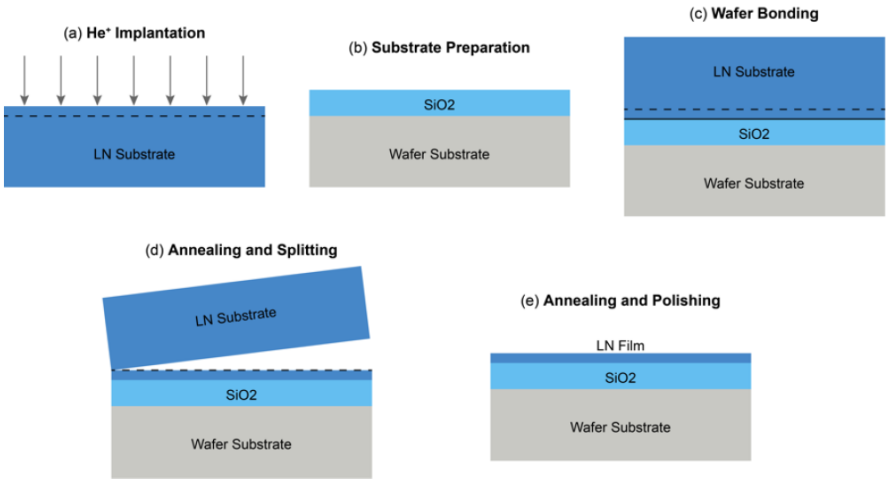


Figure 2: Schematic of the Smart Cut process for a LNOI wafer. taken unchanged from [1]

In figure 2 (a), we can see the ion implantation taking place. Commonly used ions for this are He^+, as shown in the figure, or H^+, because they are light [1][2]. The ions are implanted into a bulk LN crystal at a controlled depth, which determines the final film thickness [1]. At this chosen depth, the ions create a cleavage plane, where the crystal is weakened due to defects created by the high dose ion implantation [1]. Simultaneously the wafer substrate is prepared, which is typically LN or silicon with an oxide layer (SiO2) [1]. The thin layer is then bonded to the wafer substrate, using mature bonding methods, while still being attached to the bulk LN [2].

The caused crystal damage results in a different subsequent etch rate or thermal properties compared to undamaged bulk LN, which then allows the thin layer to be separated comparatively easy from the bulk LN with simple etching methods, such as hydrofluoric acid (HF) etching [2].
After separating the thin film and removing the rest of the bulk LN, this leaves a thin LN layer on top of the oxide layer.

2.3 LN Waveguides and fabrication methods

LN waveguides can be grouped into three main types. There are waveguides formed by in-diffusion into bulk LN, which only yields small refractive index changes and weak light confinement [1]. Commonly used are hybrid waveguides, where additional materials are

on top of LN to guide light [1]. The above mentioned waveguides will be described briefly for the sake of completeness, but for this thesis relevant is the third type of waveguides, the monolithic ridge/rib waveguides on thin-film LNOI, where the waveguides are directly etched into TFLN.

Diffused Waveguides are mostly fabricated by Titanium in-diffusion or proton exchange [1]. For Titanium in-diffusion, Ti strips are deposited on bulk LN substrates and through thermal annealing, Ti ions are diffused into the LN, causing a slightly increased refractive index in the region where Ti ions are present [1]. To fabricate waveguides by proton-exchange, the LN is immersed into a liquid source of hydrogen and protons (H^+) replace lithium ions at moderate temperatures of about 150-400 °C, causing a refractive index increase mainly for the extraordinary direction [1]. Other methods for weakly guiding diffused waveguides include ion implantation of other materials and laser writing [1]. These waveguides are unsuitable for dense integration, unable to realize micro-resonators and challenging to perform dispersion engineering, because of low index contrast of $\Delta n \approx 0.001 - 0.1$ [1]. Such index contrast results in weak optical confinement with a mode area of 10 to 100 μm^2 and large bending radii in the order of mm [1].

Hybrid waveguides avoid etching LN by placing a higher-index material strip on LN, where light is then partly confined in LN and partly in the added strip [1]. Used materials usually have similar or higher refractive index as LN, but are easier to deposit or etch [1]. Since LN is not etched, this method is often easier in fabrication, while still having access to LN's EO and nonlinear properties [1]. This method also has some limitations like weaker confinement than fully etched structures and more complex material stacks [1].

Monolithic waveguides are etched directly into TFLN enabling much higher index contrast (≈10 times larger than for ion-diffused waveguides), leading to strong confinement and compact device footprints [1]. The most common structure for these kind of waveguides are ridge or rib waveguides with a remaining slab layer and slanted sidewalls [1]. Most TFLN platforms use LN films with thicknesses of about 300-700nm, which is thin enough for strong optical confinement when patterned into ridge or rib structures [11]. One way to create these waveguides is mechanical patterning, where precision diamond-blade dicing can produce high-aspect-ratio ridges with low loss [1]. This method is not usable for creating complex layouts like grating couplers, crossings or tapers [1]. Chemical-mechanical polishing, or CMP, is able to create very smooth waveguides with sub-nanometer roughness and reported propagation loss as low as $0.027 dB/cm$ and has already been used for devices like beam splitters and Mach-Zehnder interferometers [1].

Another key technique for forming 3D structures in LN is dry etching, which uses plasma that combines chemically reactive species with ion bombardment [2]. Three main approaches were demonstrated during the past decades for dry etching, one being plasma

of pure halogen ions (like SF_6, CF_4 and BCl_3), where chemical reactions with Li create byproducts that can remain on the surface and degrade device performance and therefore sometimes require post processing like wet etching [2]. For example there is fluorine-based reactive ion-etching (RIE), which is able to successfully remove LN by forming volatile, fluorinated Nb species [1]. This specific method also forms lithium fluoride, resulting in severe redeposition problems [1]. LiF being highly resistive to further etching makes this difficult to work with and increases sidewall roughness and scattering loss [1]. The second common approach is mixing halogen ions with argon (Ar) in the plasma, which combines chemical etching with physical sputtering, where Ar ion-based etching is a pure physical bombardment process [2]. By tuning the gas ratios, etch rate, profile and surface quality can be improved, but chemical byproducts remain an issue [2]. The last demonstrated method is pure Ar plasma and it's purely physical sputtering [2]. This method yields slower etch rate but produces smooth surfaces, nearly vertical sidewalls and ultra-low propagation loss resulting in wide use for photonics device fabrication [2]. To improve etch selectivity and pattern fidelity for dry etching, hard masks are typically used in addition to photoresist [2].

Wet etching can be utilized for simpler and more economical fabrication with generally higher etch rate and smoother surfaces than dry etching [2]. A common etchant is a mixture of HF and nitric acid (HNO_3), which is often combined with proton exchange, which increases etch rate in modified regions and enables selective patterning [2]. Commonly faced problems with wet etching are shallow etching depth, sloped sidewalls and under etching [2]. Adjusting the used chemical composition of adipic acid and lithium compounds can optimize the aspect ratio D/H, where D is the etched depth and H the horizontal distance of the slant [2]. By using annealing, the mask adhesion can be improved and the problem of under etching can be reduced [2]. Some researchers have also shown, that adding some ethanol to the mixture can improve on surface smoothness [2]. Similar to proton exchange, ion implantation can also be used as a selectivity method, where damaging the crystal structure causes increasing local etch rate [2].

Other non-traditional or hybrid techniques are also used, mainly based on physical material removal [2]. One example for a method is the usage of focused ion beam (FIB) milling, enabling high precision [2]. This approach is suitable for prototyping, but too slow and expensive for large-scale fabrication [2]. Another very promising technique is a combination of femtosecond laser micromachining and polishing by FIB or chemomechanical polishing (CMPL) [2]. This technique starts with laser ablation usually performed in water to reduce the possibility of debris and cracks [2]. Ablation is then followed by surface polishing by FIB or CMPL and lastly partial wet etching of underlying layers [2]. This method enables extremely high-quality structures, where microresonators with Q-factor of about 10^8 have been demonstrated [2].

2.3.1 Ridge/rib waveguides on LNOI

Ridge (or rib) waveguides on LNOI are typically formed by partially etching the LN thin film to define a raised ridge that laterally confines the mode while the BOX and cladding provide vertical confinement [10][12]. A fabrication process of such a ridge waveguide can be seen in figure 3. The basis forms a X-cut LNOI wafer with a $400nm$ LN film on $2\mu m$ SiO_2, on top of which a $600nm$ thick layer of chromium (Cr) is deposited as a hard mask [12]. This Cr layer is then patterned using femtosecond laser ablation in water and laser parameters are tuned in a way to remove Cr without damaging the LN layer [12]. With the hard mask patterned correctly, chemo-mechanical polishing using a silica slurry and soft cloth was used to remove LN in areas that are not protected by a Cr layer [12]. The side wall angle can be controlled via polishing duration and after polishing, the Cr mask is chemically removed, followed by a final gentle polishing to improve surface roughness [12].

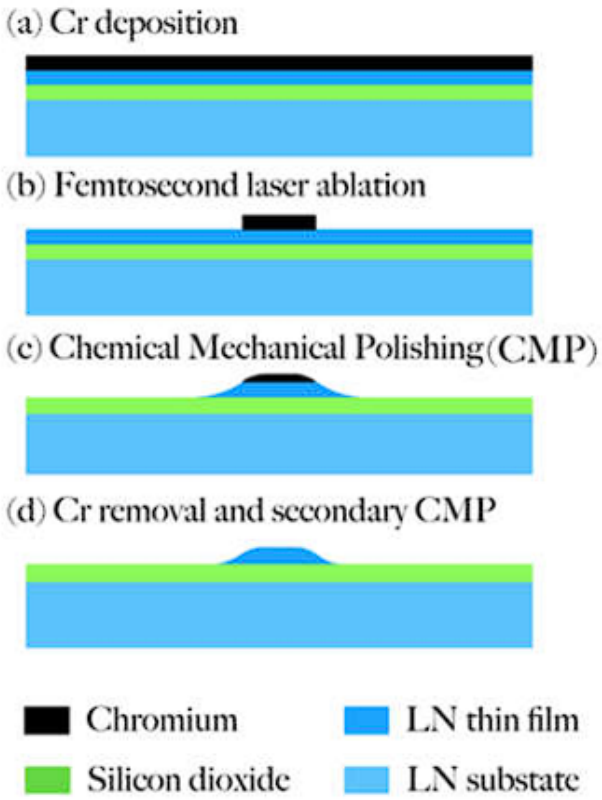


Figure 3: (a)-(d) Flow-chart of fabrication of lithium niobate on insulator (LNOI) waveguide. Taken unchanged from [12]

For a wavelength of $\lambda = 1550nm$, which is a typical telecommunication wavelength, a thickness of $600nm$ is commonly used for the TFLN layer [10]. Perfectly vertical sidewalls are mostly not achievable, with a typical value of $\phi = 30°$ for the sidewall angle [10]. The trapezoidal geometries of ridge waveguide cores allow low-loss (as low as 0.027 dB/cm),

tightly confined single-mode operation over centimeter-scale propagation lengths, which is crucial for integrated photonic circuits [10][12]. While this is a commonly used technique for waveguide fabrication on LNOI, the technique used for the devices in this work is the one in the following chapter.

2.3.2 Fabrication of fully etched LNOI waveguides

The photonic devices investigated in this work were fabricated on commercially available X-cut lithium-niobate-on-insulator (LNOI) wafers consisting of a 300 nm thick lithium niobate (LN) device layer bonded to a 4.7 μm thick silicon dioxide (SiO_2) buried oxide layer on a silicon substrate [13] [14]. The waveguide layouts are first defined by electron-beam patterning lithography (EBPL) using a spin-coated negative-tone electron-beam resist [13][14]. The exposed resist subsequently serves as an etching mask during the pattern transfer into the lithium niobate layer.

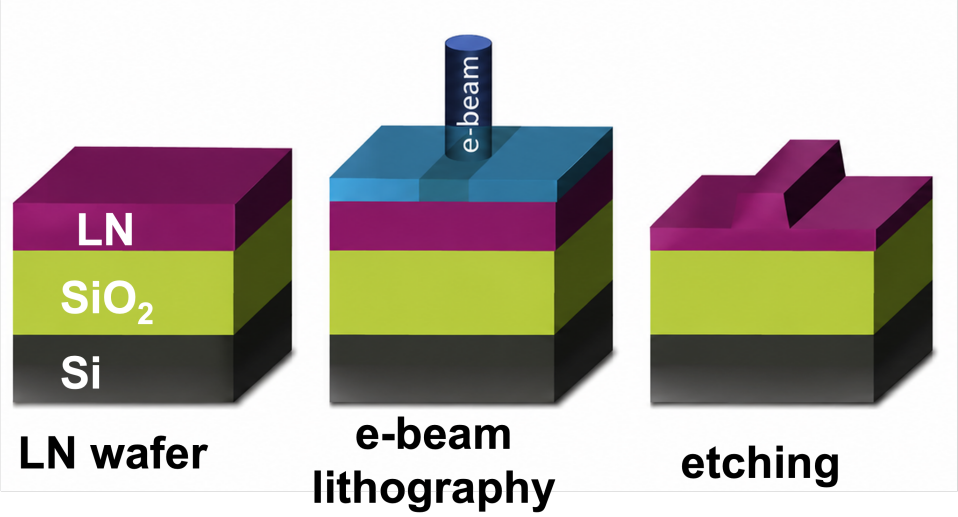


Figure 4: Fabrication steps of fully etched LNOI waveguides. Taken from [14].

The waveguide structures are transferred into the lithium niobate film by inductively coupled plasma (ICP) etching [13][14]. In this process, energetic argon ions physically sputter the exposed lithium niobate, removing material from the unprotected regions while the resist mask preserves the desired waveguide geometry [13][14]. Since the etching process is based predominantly on physical sputtering, redeposition of lithium niobate can occur on the etched surfaces and sidewalls. To remove this redeposited material, the sample is first treated using a potassium hydroxide (KOH) solution followed by an RCA-1 cleaning process [13][14]. Finally, the fabricated devices are annealed at 400°C to improve the optical transmission of the waveguides [13][14].

The ring resonators investigated in this thesis are fabricated as fully etched strip waveguides, where the lithium niobate layer is completely removed down to the underlying silicon dioxide layer outside the waveguide core. This geometry provides strong optical confinement while leaving the waveguide surface directly accessible for post-fabrication processing, such as the localized electron-beam-induced carbon deposition, which will be further investigated in this work.

Although modern nanofabrication techniques enable the realization of high-quality LNOI waveguides with low propagation losses, each fabrication step inevitably introduces small process variations. During electron-beam lithography, factors such as dose variations, resist development, and line-edge roughness can lead to deviations from the intended geometry, while the subsequent ICP etching process may introduce variations in etch depth, sidewall angle, sidewall roughness, and local material redeposition. In addition, wafer-scale variations in the thickness and uniformity of the lithium niobate and buried oxide layers can further contribute to device-to-device differences. Since the optical properties of LNOI waveguides are highly sensitive to their geometry and material composition, even nanometer-scale deviations can alter the effective refractive index, resonance wavelength, propagation loss, and quality factor of photonic devices. These unavoidable fabrication-induced variations motivate the development of post-fabrication trimming techniques capable of restoring or fine-tuning the optical response of individual devices.

2.4 Guided modes

A guided mode in LNOI waveguide is characterized by an effective refractive index n_{eff} that lies between the refractive index of the core and that of surrounding claddings [15][12]. The effective index describes not only the phase velocity of the guided mode, but also the propagation direction and it is used to compute quantities like free spectral range and attenuation coefficient in LNOI microrings and waveguides [12]. Guided modes in LNOI ridge waveguides show exponential decay outside of the core depending on the refractive index of BOX or cladding. [15]. Since the guided mode is not fully confined to the high-index core, its evanescent tail extends into BOX and cladding and changing either one will directly perturb the modal field and propagation constant [16][17][18].

The core is the TFLN and it provides not only the high refractive index, but also EO and nonlinear properties and is the main region of optical confinement with support for TE and TM modes [12][15]. The BOX is defined by the SiO_2 layer on which the TFLN rests on and it has a significantly lower refractive index compared to LN [12]. This results in a vertical index contrast, that isolates the guided mode from the substrate and reduces leakage and bending loss [12]. Lastly top cladding, which can be just air or a deposited dielectric,

controls the symmetry of the vertical mode profile, confinement factor in the core and scattering losses at etched sidewalls, depending on the refractive index and thickness of the top cladding [12]. This combination of core, BOX and top cladding determine the effective index, cutoff conditions and single-mode windows of LNOI ridge waveguides [15].

Changing the refractive index, thickness or composition of the top cladding modifies how much of the modal field resides in the cladding compared to the core and also tunes sensitivity to absorption or scattering in that region [18][19].
According to first-order perturbation theory, small modifications of the refractive index in the top cladding will cause a shift of the propagation constant and n_{eff} [20][21]. The change in n_{eff} is proportional to the evanescent field energy in the altered cladding. [20][21]. Increasing the top-cladding index generally reduces vertical index contrast between core and cladding, which leads to weaker vertical confinement, enlarges mode size and can lower bend-loss limits [22][19]. Not only that, but changes in the cladding also modify the wavelength dependence of n_{eff}, because the fraction of modal field in each material shifts as a function of wavelength and cladding index [20][22]. Changes to the top-cladding can differently affect quasi-TE and quasi-TM modes in LNOI specifically, because their evanescent tails sample the cladding with different strengths, leading to polarization-dependent changes in confinement, propagation losses and dispersion [18]. Therefore, depositing carbon on the waveguide changes the effective index by perturbing the evanescent field.

2.5 Important understanding for racetracks

The following equations are used throughout the Results to quantify trimming performance.

The refractive index, assuming there is homogenous refractive index in the whole racetrack, can be calculated with the free spectral range (FSR), the vacuum wavelength λ and the total path length of the racetrack L_{tot} as follows:

$$n_{eff} = \frac{\lambda^2}{FSR \cdot L_{tot}} \tag{2}$$

If the full width half maximum (FWHM) of the resonance is small, the loaded Q-factor can be approximated using

$$Q_L = \frac{\lambda}{FWHM} \tag{3}$$

where λ is the wavelength of resonance in the spectrum of a resonator. A more accurate

form to calculate the loaded Q-factor even for bigger FWHM is

$$Q_L = \frac{c/\lambda}{c(\frac{1}{\lambda - FWHM/2} - \frac{1}{\lambda + FWHM/2})} \tag{4}$$

where c is the vacuum velocity of light. With the loaded Q-factor, the intrinsic Q-factor can be calculated by

$$Q_I = \frac{2Q_L}{1 \pm \sqrt{T}} \tag{5}$$

where T is the measured transmission intensity at the resonance. Plus or minus in the equation is chosen for under or over coupling respectively. By calculating the equivalent radius for microring resonators with the same L_{tot} as the racetracks

$$R_{equi} = L_{tot}/2\pi \tag{6}$$

one can calculate the propagation loss of the resonators in $[\frac{dB}{cm}]$ with

$$\alpha = \frac{\lambda \cdot 4.34 \cdot 10^4}{FSR \cdot Q_I \cdot R_{equi}} \tag{7}$$

Since a part of the waveguide, where carbon is deposited, has different effective refractive index than the rest of the waveguide, equation (2) is not a perfect representation for the effective refractive index in every part of the resonator. To approximate the propagation loss in the trimmed section of the resonator, the trimming length and the propagation loss of an untrimmed resonator with the same dimensions are needed as additional information. Using that

$$\alpha_{trim} = \frac{\alpha \cdot L_{tot} - \alpha_{untrim} \cdot L_{untrim}}{L_{trim}} \tag{8}$$

can be approximated, where $L_{untrim} = L_{tot} - L_{trim}$. Similarly, the effective refractive index can be approximated using the effective refractive index of an untrimmed resonator and

$$n_{eff,trim} = \frac{n_{eff} \cdot L_{tot} - n_{eff,untrim} \cdot L_{untrim}}{L_{trim}} \tag{9}$$

This is only an approximation, where it is assumed that all resonators with the same dimensions behave the same. This is not the case in reality due to small differences in fabrication leading to differences in geometry or material composition.

3 Experimental methods and setup

The general experimental strategy to investigate carbon deposition for LNOI waveguides is an iterative workflow between deposition and evaluation. Each processing step was followed by optical characterization to decide the next action. This means, that first untrimmed racetrack resonators were measured as reference and measured again after trimming to identify trimming induced changes. Depending on what different recipes yield for Q-factor, resonance shifts or propagation loss, measurement protocol and recipe were changed to find viable conditions for carbon deposition on LNOI waveguides. In short, a feedback based decision chain was used:

$$\boxed{\text{Measure}} \rightarrow \boxed{\text{Trim}} \rightarrow \boxed{\text{Measure}} \rightarrow \boxed{\text{Evaluate}} \rightarrow \boxed{\text{Next recipe}}$$

3.1 Photonic devices and laboratory setup

In this thesis, racetrack resonators on LNOI photonic platforms, as seen in figure 5, will be trimmed. The dimensions of the resonators are also seen in that figure.

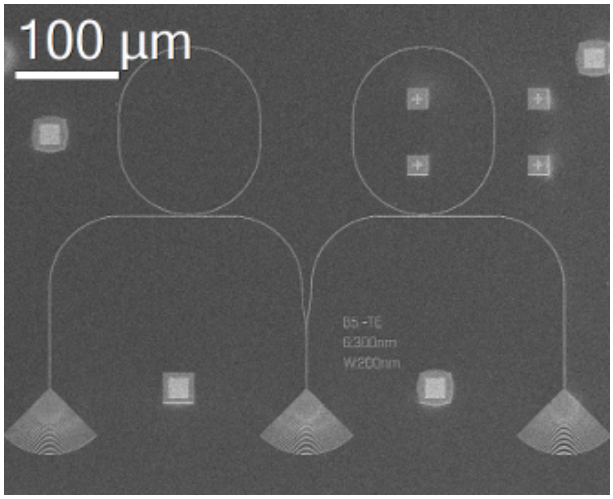


Figure 5: LNOI Racetrack resonators.

The devices are composed of three grating couplers, which are connected with two racetrack resonators. The racetracks are composed of two half circles with a radius of $70\mu m$ and two straight sections of length $25\mu m$, which will be trimmed. Light at the wavelength of around 1550nm is fed from a laser into a fiber array and is input in the middle grating coupler, where the light is then split up into both sides of the device by a multimode interferometer. Before inserting the laser light, it is polarized such that the measured intensity at the output grating couplers is maximized. Around half of the light will be coupled into the racetrack and channelled back into the waveguide, which leads to a phase

shift between light in the waveguide and light coming from the racetrack. This phase shift is dependent on the optical path the light needs to cover in the racetrack, which is influenced by the effective refractive index and the length of the geometrical path that forms the racetrack.

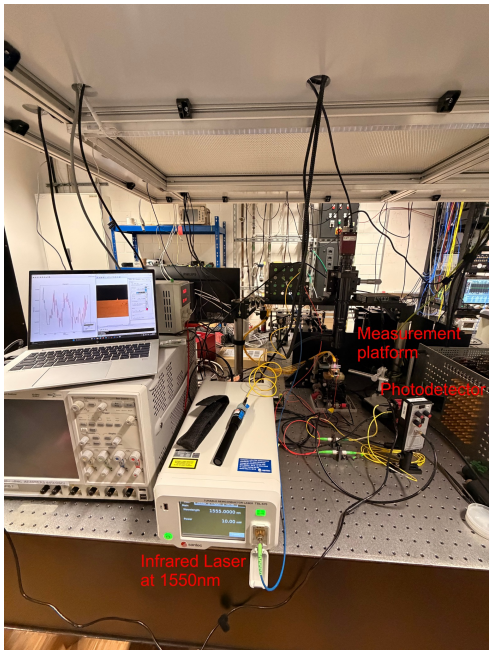
The laboratory Setup can be seen in Figure 6 and the measurement procedure consists of the following steps:

- **Place and fix the chip:** The chip containing the etched devices is placed on the measurement platform shown in Figure 6 (b) and fixed in position using an air pump. This figure also shows other important measuring components that will be addressed later.
- **Adjust the platform height:** The height of the platform is adjusted so that the chip is positioned as close as possible to the fiber array without touching it. This ensures an appropriate vertical alignment between the grating couplers and the fiber array.
- **Align the grating couplers with the fiber array:** Since the chip may not initially be positioned such that the grating-coupler row is parallel to the fiber array, the platform is rotated while observing the chip with the microscope camera. The rotation is adjusted until the grating couplers and the fiber array are parallel.
- **Assign the fiber-array channels:** For clarity, the five fiber-array channels are numbered from 1 to 5, from left to right. The grating-coupler spacing is defined during chip fabrication such that one fiber-array channel is positioned between two couplers, while the neighboring channels are positioned above the couplers.
- **Define the optical channels:** Channels 1 and 5 are connected to photodetectors to measure the optical output from the outer grating couplers. Channel 3 is connected to the laser source and is used to couple laser light into the central grating coupler.
- **Select an alignment channel:** Either channel 2 or channel 4 is used as a fixed reference point for positioning the fiber array. An alignment laser operating in the visible spectral range is connected to the selected channel.
- **Position the fiber array using the alignment laser:** The position of the alignment laser spot is monitored with the microscope camera and adjusted until it is placed between two grating couplers, such that the three grating couplers are aligned with channels 1, 3, and 5.
- **Move the chip relative to the fiber array:** The relative position of the fiber array and the chip is adjusted by moving the platform on which the chip is fixed.

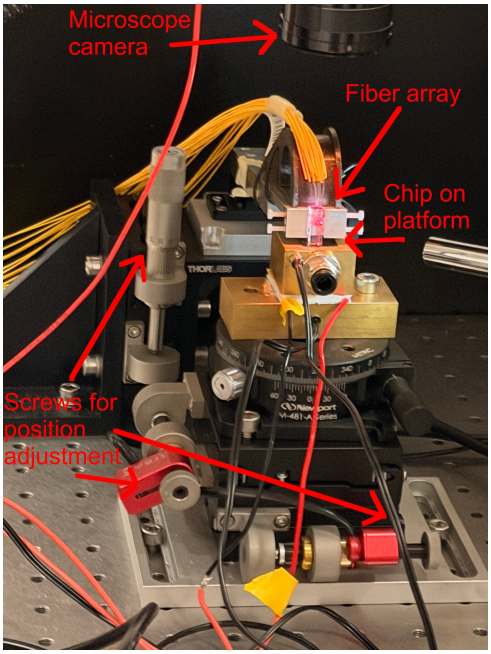
Coarse adjustments are performed manually, whereas fine adjustments are performed using motorized stages controlled by a program on the laboratory computer.

- **Optimize the coupling position:** The optimum position of the fiber array is determined by monitoring the intensities measured by the photodetectors. The position is adjusted until the maximum optical intensity is measured at one of the photodetectors.
- **Measure the resonator spectra:** Once the fiber array is correctly positioned, the resonators are measured by sweeping the laser wavelength over the range from 1540 nm to 1560 nm and recording the corresponding intensity.
- **Save the measurement data:** The measured spectrum is displayed using the software on the laboratory computer like its shown in Figure 6 (c). The corresponding wavelength and intensity values are saved in a text file for subsequent analysis.

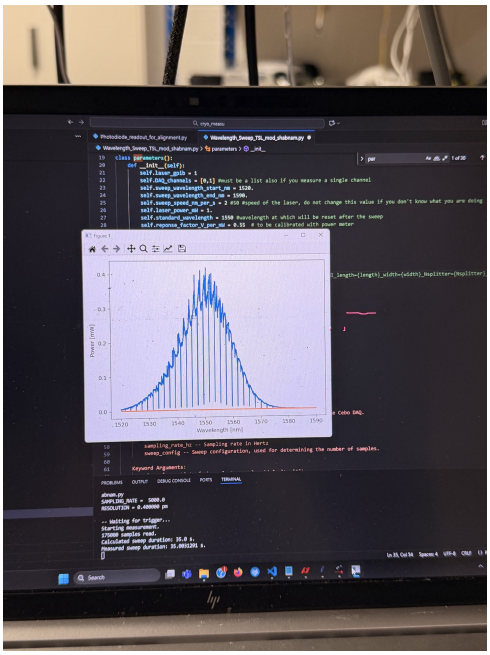
While sweeping, a spectrum with extinction lines, where the light from the racetrack has the opposite phase from the light in the waveguide, can be measured at both output grating couplers. Depending on the change of the effective refractive index inside of the waveguide, these extinction lines will occur at different wavelengths in the spectrum. By measuring the Q-factor and position of the extinction lines before trimming, evaluating how much different parameters in trimming affect the Q-factor and the wavelengths of extinction lines of this spectrum is possible. To do that, the devices were first measured without any carbon deposition and the spectra are evaluated. The devices are then trimmed and measured again multiple times after different time intervals and changes are evaluated for arbitrary extinction lines.



(a)



(b)



(c)

Figure 6: (a) Laboratory setup (b) Chip measurement platform (c) Measured spectrum for a device.

With the following trimming methods, it should be possible to influence the effective refractive index of the waveguide of the racetrack, which will change the resulting Q-factor and phase shift.

3.2 FIB assisted carbon deposition

FIB assisted carbon deposition served as the initial benchmark because it had previously been successful on SiN and it will be explained here in more detail. In this technique, a focused ion beam is used to locally decompose precursor gas molecules, enabling precise deposition of diamond-like amorphous carbon [3]. The trimming process starts with directing the carbon-containing precursor gas toward the waveguide through a gas nozzle. This precursor gas is then targeted near the waveguide by the FIB, which contains Ga^+ ions. These ions induce local decomposition of the precursor gas molecules, leading to an accumulation of carbon in the irradiated region of the waveguide. Using this method, precision can be achieved on a nanometer scale [3].
This method was used in 2025 to trim asymmetric directional couplers (A-DC), where Carbon was deposited on the narrow waveguide of the A-DCs to control the effective refractive index of the TE_0 mode.
Similar to the procedure used for the racetrack resonators, light is input into a grating coupler and then split by a multimode interferometer. As seen in in Figure 7 d),e),g) and h), the insertion losses are dependent on the widths of the waveguides in the region of mode conversion.

It was shown that the deposited carbon has not only negligible effect on the field distribution of the TE_0 mode, because of its small geometric dimensions and moderate refractive index, but also that both carbon and gallium are only localized in the deposition area without intruding into the SiN waveguide [3]. This type of deposition also does not cause a change in the collective electronic response of the material and the deposition is confined to this region and no significant structural alterations are detectable, showing the non-volatile behaviour of this method [3].

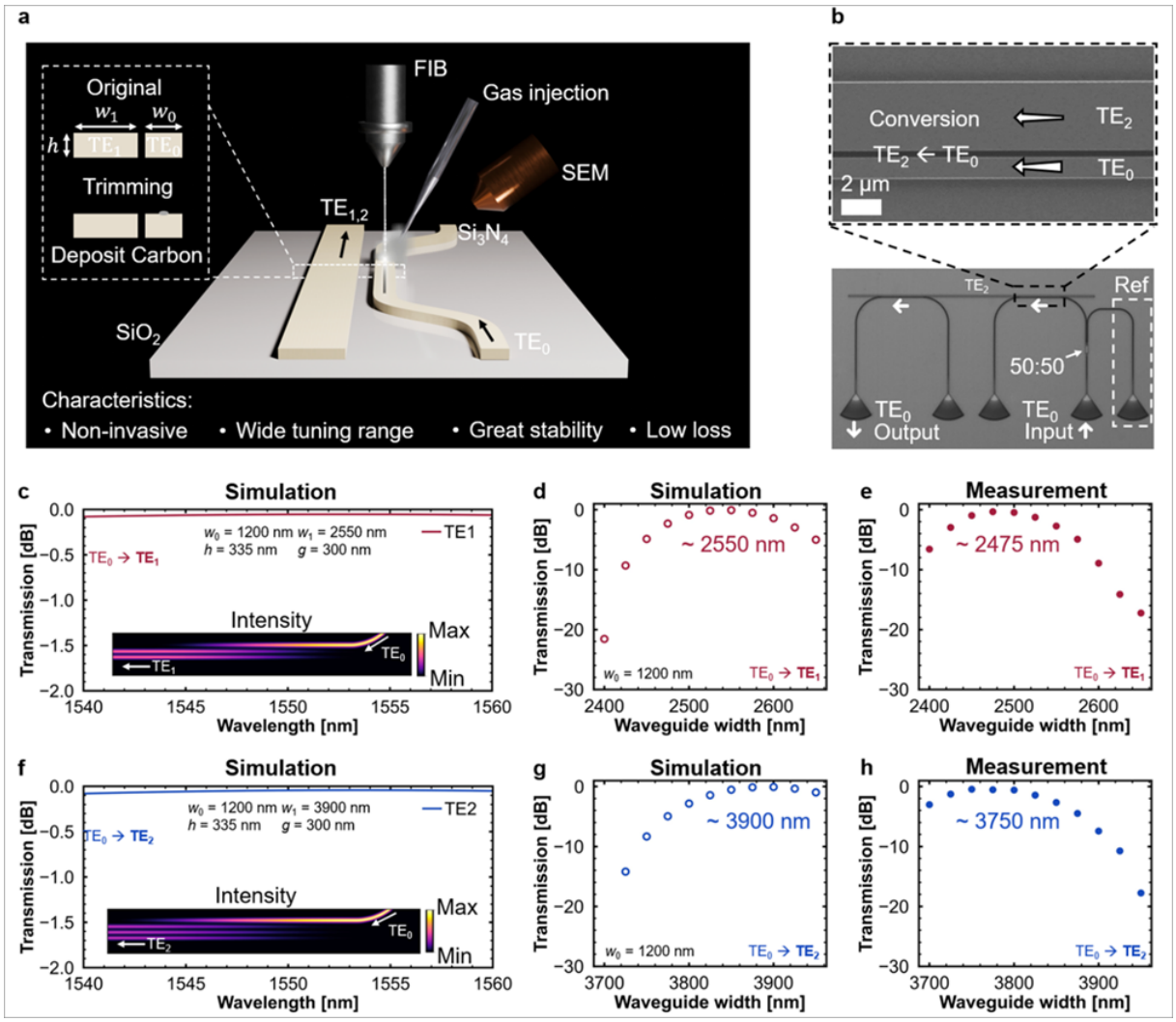
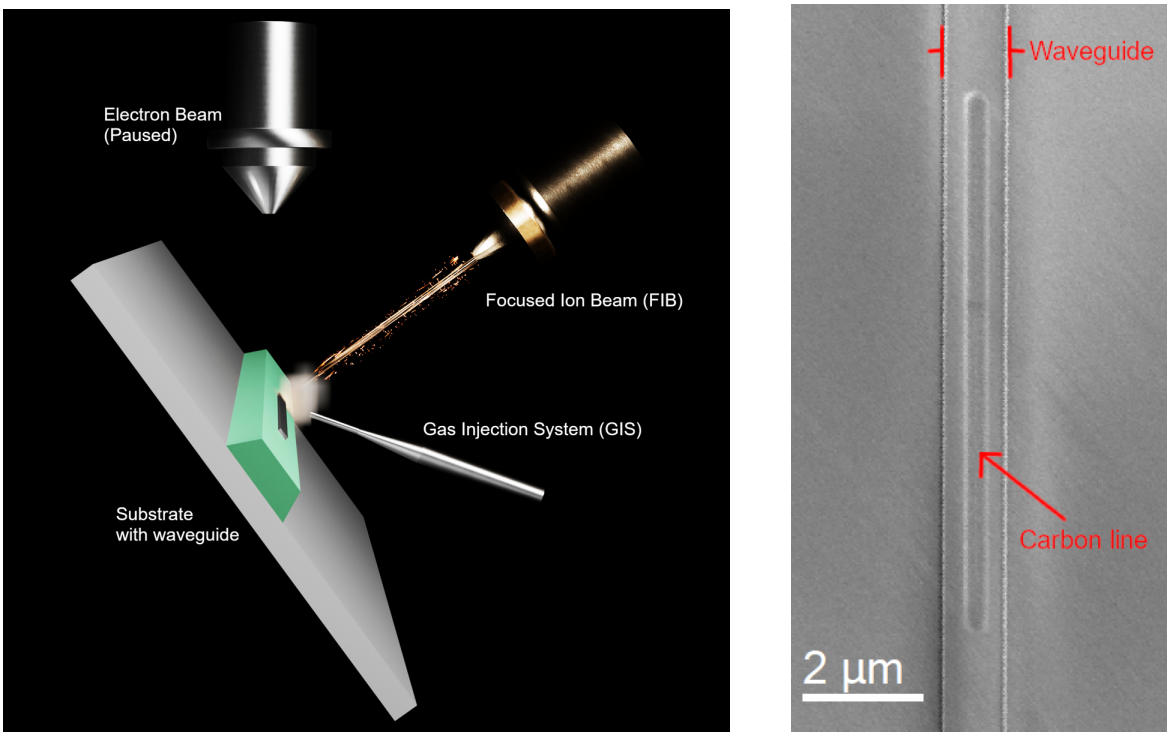


Figure 7: Schematic diagram of a trimmed A-DC using carbon deposition, and the transmission response of the untrimmed A-DCs. a) Schematic of a trimmed A-DC by carbon deposition. b) Images of a fabricated A-DC for mode conversion between TE0 and TE2 modes. c) Simulated transmission spectrum and intensity distribution of the TE1-mode A-DC. d), e) Simulated and measured transmission of the TE1-mode A-DCs with increasing w1. The difference between the simulation results and the measurement results is due to fabrication errors in the width of the waveguides. f) Simulated transmission spectrum and intensity distribution of the TE2-mode A-DC. g), h) Simulated and measured transmission of the TE2-mode A-DCs with increasing w1. Taken unchanged from [3].

The setup used in this thesis is shown in Figure 8 (a). The substrate on which the waveguide sits atop is brought into the setup, where both of the trimming techniques in this thesis can be performed. Like in the publication [3], the precursor gas is brought to the waveguide via a Gas Injection System (GIS), where the Gas molecules are then deposited using a Focused Gallium Ion (Ga^+) Beam. While closely monitoring the waveguide and deposition through a SEM, a fine line of Carbon can be deposited on the waveguide as seen in Figure 8 (b).



(a) (b)

Figure 8: (a) Deposition Setup for FIB (b) Waveguide after carbon deposition using FIB seen through SEM.

3.3 EBeam assisted carbon deposition

Similar to FIB assisted carbon deposition, the focused electron beam induced deposition (FEBID, here often referred to as just EBeam assisted deposition) is a direct-write nanofabrication technique [23]. FEBID was expected to cause less structural damage because no Ga implantation occurs. For this technique a precursor gas is again delivered to the waveguide via a gas injection system under observation through an electron microscope [23]. There, the molecules of the gas are dissociated locally by a focused electron beam, leaving a non-volatile deposit while volatile fragments desorb [23]. During irradiation, the precursor continuously adsorbs and is replenished [24]. The dissociation is primarily driven by low-energy secondary electrons and not the primary beam itself and multiple dissociation channels exist, which have strongly energy- and precursor-dependent cross sections [23]. Therefore growth behaviour strongly depends on precursor properties like vapor pressure, adsorption characteristics and stability on the substrate and surface dependent decomposition or instability [23]. There are many important surface processes happening during deposition like adsorption, surface diffusion, residence time, thermal- and electron-stimulated desorption [23].

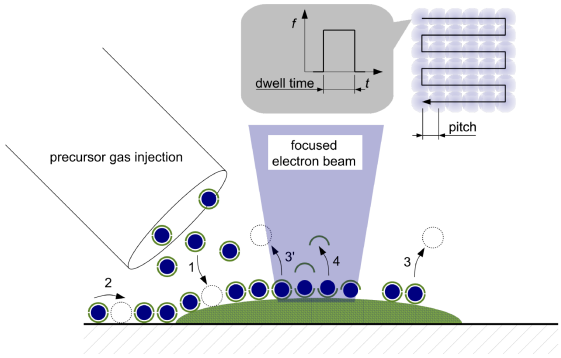
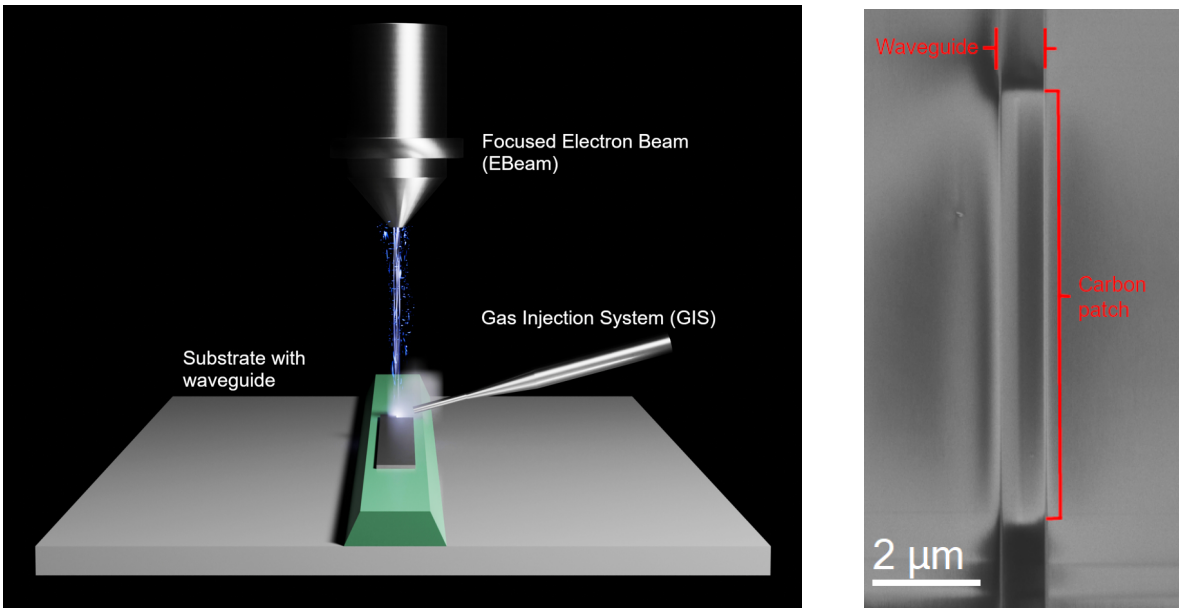


Figure 9: Illustration of FEBID. Precursor molecules are supplied by a gas-injection system and physisorb (1) on the surface. Surface diffusion (2), thermally induced desorption (3) and electron-stimulated desorption (3') take place. Within the focus of the electron beam, adsorbed precursor molecules are (partly) dissociated followed by desorption of volatile organic ligands (4). Upper right: For pattern definition the electron beam is moved in a raster fashion over the surface and settles on each dwell point for a specified dwell time. After one raster sequence is completed the process is repeated until a predefined number of repeated loops is reached. Taken unchanged from [24].

Final deposition composition depends on both precursor chemistry and beam parameters, where some systems can be highly sensitive while others are comparatively robust [23]. The key writing parameters are beam energy or acceleration voltage, probe current, dwell time t_D, pixel pitches p_x and p_y, precursor flux and scan strategy [23]. Patterning can then be achieved by rastering the beam and repeating scan loops to build thickness [23]. The primary beam has a Gaussian spatial profile with a common value of $FWHM \approx 2.36a$ and secondary electrons with 1-10eV peak dominate dissociation due to higher cross sections at low energies, but the lateral spread of those electrons limit resolution to about $3nm$ features [24]. Electrons penetrate deeply to a depth of $\approx 100nm$ at 5keV, which leads to continuous irradiation of already deposited material [24]. Embedded precursor fragments can still dissociate post-growth and post-irradiation can be used to tune properties like electrical conductivity [24].

For the EBeam deposition in this thesis, the substrate with waveguide is again brought into the trimming setup that was already used for FIB deposition. This time the FIB is paused and the focused EBeam is activated as can be seen in Figure 10 (a). Compared to FIB, Figure 10 (b) shows a wider patch of carbon, that covers an entire section of the waveguide, instead of a fine line.



(a) (b)

Figure 10: (a) Deposition Setup for EBeam (b) Waveguide after carbon deposition using EBeam seen through SEM.

3.4 Evaluation procedure

The measured spectra are analysed using a Python script. The evaluation procedure follows the sequence

$$\boxed{\text{spectrum}} \rightarrow \boxed{\text{peak finding}} \rightarrow \boxed{\text{FWHM}} \rightarrow \boxed{\text{Q-factor}} \rightarrow \boxed{\text{propagation loss}}$$

The individual evaluation steps are:

- **Spectrum input:** The device parameters are provided to the Python script as an array and the measured spectra are imported from text files.
- **Spectrum preprocessing:** If a spectrum is not already normalized, a Savitzky-Golay filter is applied to reduce measurement noise. Then, the spectrum is normalized.
- **Peak finding:** The extinction lines, corresponding to the resonance dips, are identified in the normalized spectrum. The spectrum is plotted with the detected extinction lines marked to verify that all resonances have been identified correctly.
- **Free spectral range:** The free spectral range (FSR) is determined from the wavelength positions of neighboring extinction lines.

- **Effective refractive index:** The full width at half maximum (FWHM) of each resonance is determined. Together with the measured FSR, the known racetrack dimensions, and Equations 2 and 9, the effective refractive indices are calculated.
- **FWHM determination:** For each extinction line, the resonance linewidth is obtained from its FWHM. The FWHM is used as the linewidth parameter for the following Q-factor calculation.
- **Q-factor calculation:** The loaded and intrinsic Q-factors are calculated from the resonance wavelength and FWHM using Equations 4 and 5.
- **Propagation-loss calculation:** The propagation loss is calculated from the extracted Q-factors using Equation 8.
- **Averaging of the Q-factor and propagation loss:** To reduce the influence of outliers and obtain a representative value for the change in Q-factor and propagation loss, a mean Q-factor and propagation loss is calculated. This mean is obtained using all quality factors and propagation losses extracted from resonances within the wavelength range from 1540 nm to 1560 nm.

3.5 Used trimming recipes

Many devices on the used chip were trimmed with different methods, intensities, trimming lengths, trimming locations and were measured over different time lengths.
This Chapter will give a short overview of what has been done to the different devices.

3.5.1 FIB

Table 1: FIB trimming recipes

Device	acceleration Voltage	probe current	thickness	length	type
C0	30kV	20pA	<200nm	3μm	FIB
C5	30kV	20pA	<100nm	4μm	FIB
C6	30kV	20pA	<200nm	4μm	FIB
C7	30kV	20pA	<100nm	5μm	FIB
C8	30kV	20pA	<200nm	5μm	FIB
G8	30kV	20pA	<100nm	3μm	FIB
G4	5kV	200pA	<200nm	3μm	FIB
G7	5kV	200pA	<400nm	3μm	FIB

3.5.2 EBeam

Table 2: EBeam trimming recipes

Device	acceleration Voltage	probe current	thickness	length	type
H3	10kV	150pA	50nm x2	10μm	EBeam
H4	10kV	150pA	50nm x2	15μm	EBeam
H5	10kV	150pA	50nm x2	20μm	EBeam
H6	10kV	150pA	50nm x2	10μm	EBeam
H7	10kV	150pA	50nm x2	10μm	EBeam
A1	10kV	150pA	50nm	5μm	EBeam
A2	10kV	150pA	50nm	10μm	EBeam
A3	10kV	150pA	50nm	15μm	EBeam
A4	10kV	150pA	50nm	5μm	EBeam
A5	10kV	150pA	50nm	10μm	EBeam
F0	10kV	150pA	50nm	18μm	EBeam
F1	10kV	150pA	50nm	16μm	EBeam
F2	10kV	150pA	50nm	14μm	EBeam
F3	10kV	150pA	50nm	12μm	EBeam
F4	10kV	150pA	50nm	10μm	EBeam
F5	10kV	150pA	50nm	8μm	EBeam
F6	10kV	150pA	50nm	6μm	EBeam
F7	10kV	150pA	50nm	4μm	EBeam
F8	10kV	150pA	50nm	2μm	EBeam

4 Results

4.1 Results for FIB recipes

First, six resonators were trimmed using FIB with a high acceleration voltage of 30kV and low probe current of 20pA. Trimming length and thickness were varied according to table 1 in section 3.5.1. In Figure 11, the difference of mean Q-factor before and after trimming relative to the mean Q-factor of the untrimmed resonator is plotted against the trimming length. As can be seen in this Figure, FIB assisted carbon deposition seems to cause considerable Q-factor reduction. It can be seen that the trimming length seems to influence the Q-factor the most, but thickness also influences Q-factor, were thicker deposition usually reduces the Q-factor more than thinner deposition.

The best device measured was the c8 device with a reduction of Q-factor of around 30%. Another device with a trimming length of $5\mu m$ showed a reduction of 40%, while two devices with a trimming length of $4\mu m$ and varying thickness both show a reduction close to $\approx 79\%$. Two devices with trimming length $3\mu m$ show slightly better results with $\approx 48\%$ reduction for a thickness of $< 100nm$ and $\approx 68\%$ reduction for a thickness of $< 200nm$.

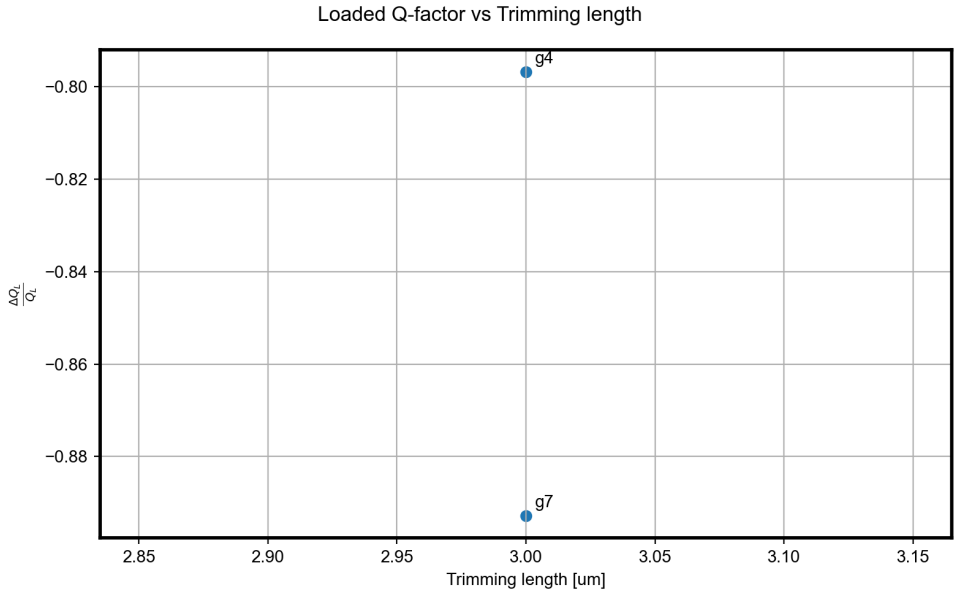


Figure 12: Q-factor change for FIB recipes. (5kV, 200pA)

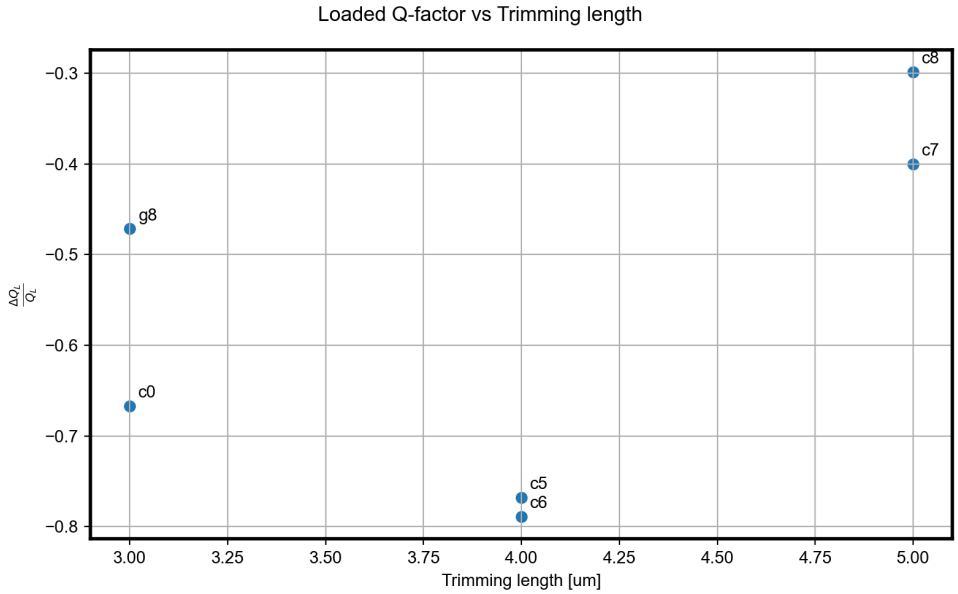


Figure 11: Q-factor change for FIB recipes. (30kV, 20pA)

Two more devices were trimmed using the FIB assisted deposition with an acceleration voltage of only 5kV and a probe current of 200pA. The Q-factor reduction can be seen in Figure 12 and it shows a reduction of $\approx 79\%$ for a thickness of $< 200nm$ and $\approx 89\%$ for a thickness of $< 400nm$. We can again see a negative impact on the Q-factor for a thicker deposited line.

Comparing high voltage and low current with low voltage and high current, one can see that using low voltage and high current seems to cause more damage in the waveguide than using high voltage and low current.

FIB assisted carbon deposition seems to cause great damage for the quality of the LNOI waveguides, contrary to what has been shown for SiN waveguides in [3].

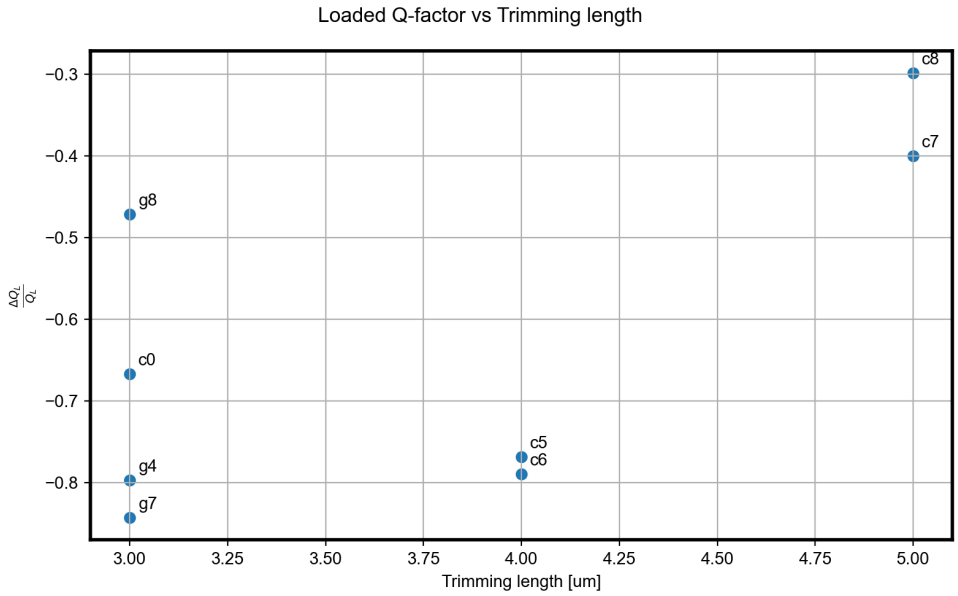


Figure 13: Q-factor change for FIB recipes.

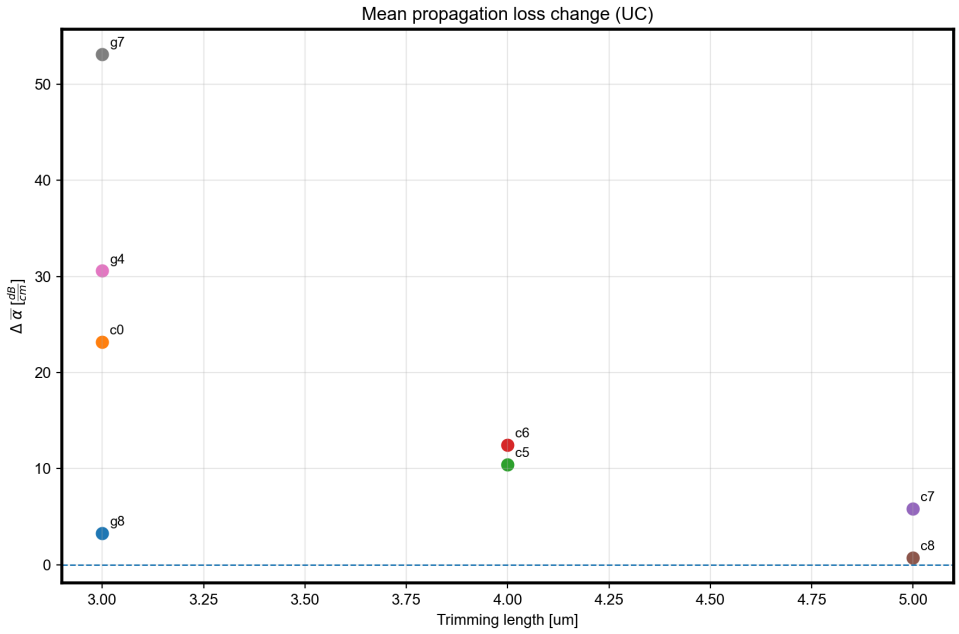


Figure 14: Mean propagation loss change for FIB devices assuming under coupling.

The propagation losses can be determined using these Q-factors and comparing propagation losses of untrimmed devices with their trimmed measurements yields Figure 14, where under coupling (UC) was assumed for calculating the intrinsic Q-factors and propagation loss. Assuming under coupling is sensible here, because under coupling means, that the external coupling rate is smaller than internal losses, which is probably the case

for these ring resonators, because there are only few structures near the resonators that could cause external coupling. Looking at the $3\mu m$ column in Figure 14, it seems that the thickness of deposited carbon correlates to propagation loss in the waveguide, since the recipe with a thickness of $< 400nm$ causes a propagation loss change of $\approx 52\frac{dB}{cm}$ and two recipes with a thickness of $< 200nm$ cause $\approx 30\frac{dB}{cm}$ and $\approx 23\frac{dB}{cm}$, respectively.

In general higher probe current seems to cause higher propagation loss for FIB, which could be caused by higher gallium in-diffusion and implantation into the waveguide causing defect formations. Not only can higher probe current increase gallium in-diffusion but also sputtering and milling of the waveguide surface will be increased, which leads to further degradation of waveguide quality. Low probe current should also keep the beam spot small and more controlled, which improves resolution and reduces collateral damage. If low probe current is desirable for FIB, acceleration voltage needs to be increased, which increases secondary electron yield from the substrate and with that keeps deposition rate practical. High voltage will in turn also increase penetration depth, which will cause defects deeper inside the waveguide, but the quality degradation caused by that seems to be less than for high probe current.

Surprisingly, a clear correlation between trimming length and Q-factor or propagation loss can not be seen in the measurements taken for the proposed FIB recipes for carbon deposition.

4.2 Results for EBeam recipes

EBeam assisted carbon deposition seems to yield considerably better results in terms of Q-factor compared to FIB, as can be seen in Figure 15. For all EBeam devices an acceleration voltage of 10kV and a probe current of 150pA was chosen. The devices in Figure 15 were trimmed twice for a thickness of $50nm$, which should result in a thickness of $100nm$, but the exact thickness could only be determined by examining the cross section of the waveguide, which is not simple. Trimmed in that way, Figure 15 only shows Q-factor reductions in ranges of 5.5% to 13%, which is a huge improvement compared to FIB. Because of this, EBeam assisted deposition seems to be the more viable option for carbon deposition on LNOI waveguides.

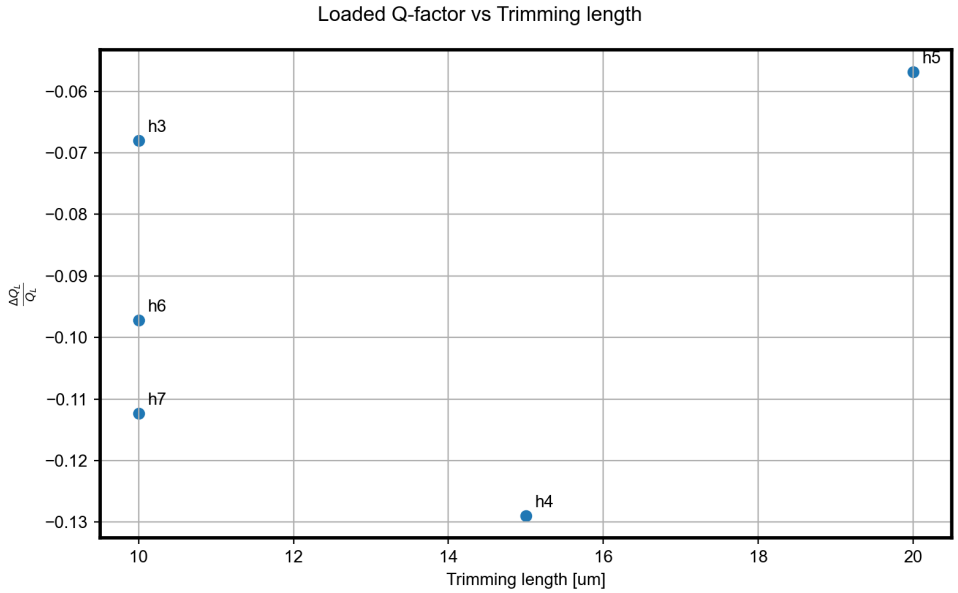


Figure 15: Q-factor change for EBeam recipes. (10kV, 150pA, 50nm x2)

This is validated by the devices in Figures 16 and 17. Devices in Figure 16 were trimmed once for a thickness of $50nm$ and show Q-factor reductions ranging from 2.5% to 7.5%. Because this reduction is lower than that for the previous devices, the double trimming or higher thickness seem to cause more damage to the waveguide than smaller thickness from one deposition process. With a thickness of again $50nm$, Figure 17 shows measurements for a variety of trimming lengths ranging from $2\mu m$ to $18\mu m$. We see again generally low reduction in Q-factor with some outliers reaching reductions of up to 22.5%, which is still better than for FIB.

The devices from Figures 16 and 17 were heat treated at $200°C$ for 30 Minutes on a regular hot plate and measured again. The results for after heat treatment can be seen in Figure 18. With heat treatment the quality of the waveguides improves greatly, causing most waveguides to be measured with Q-factor change close to zero. Only one device remains with a reduction greater than 10% and for some devices even Improvement of Q-factor is reported with one device having its Q-factor increased by almost 50% compared to the untrimmed resonator.

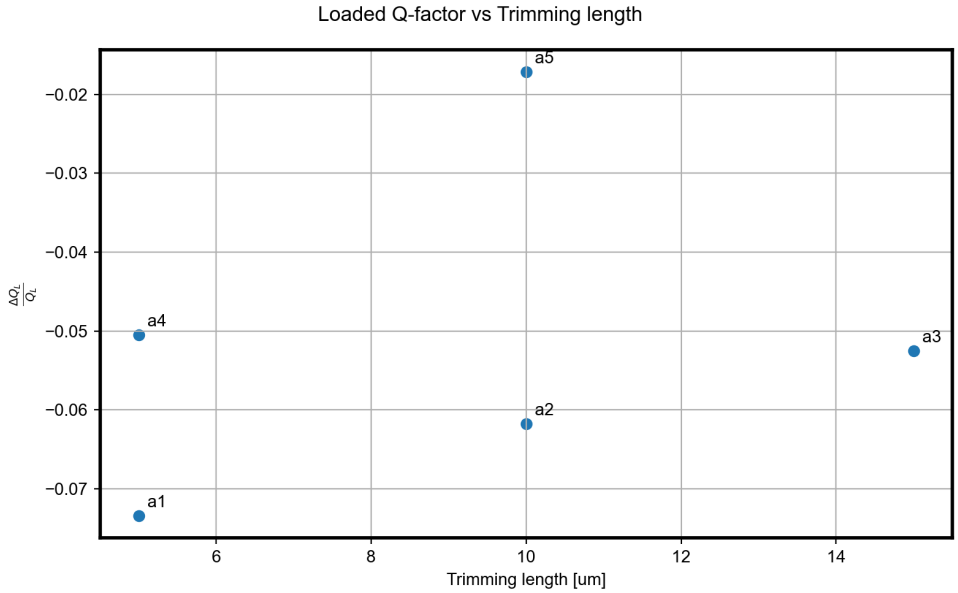


Figure 16: Q-factor change for EBeam recipes. (10kV, 150pA, 50nm)

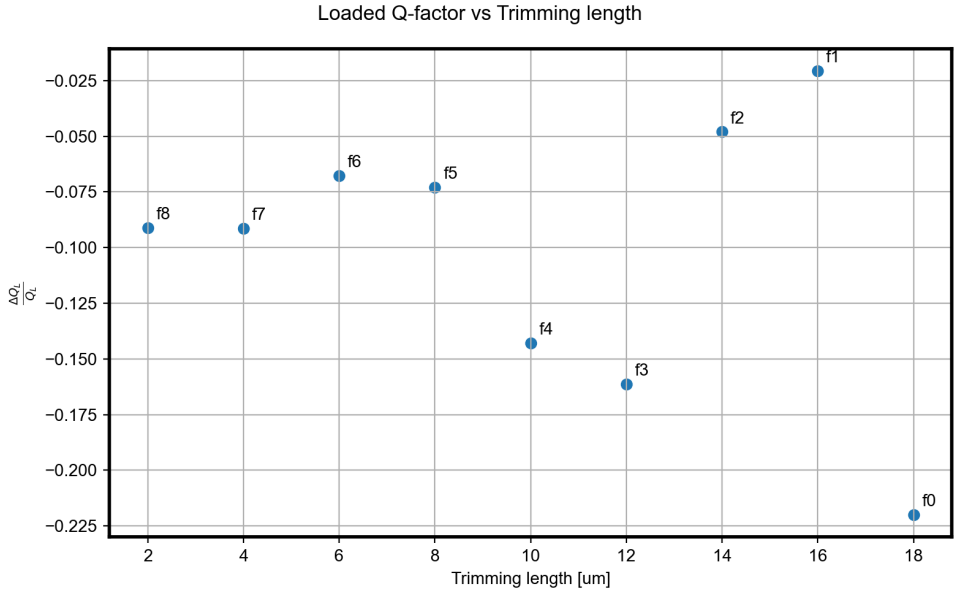


Figure 17: Q-factor change for EBeam recipes. (10kV, 150pA, 50nm)

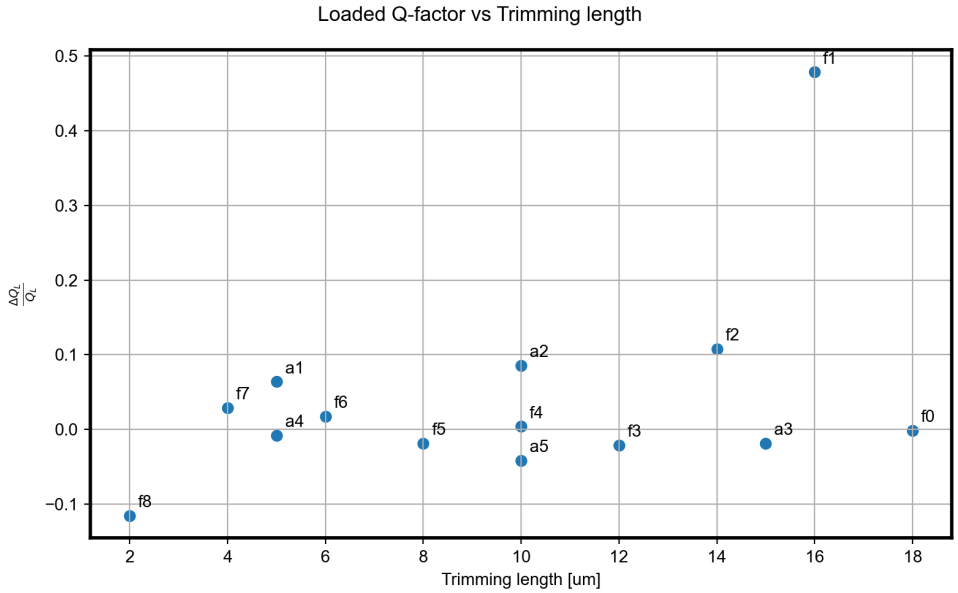


Figure 18: Q-factor change for EBeam recipes after heat treatment. (10kV, 150pA, 50nm)

The propagation losses for devices trimmed with the EBeam recipes can be determined using these Q-factors, which results in what we see in Figures 19 and 20.

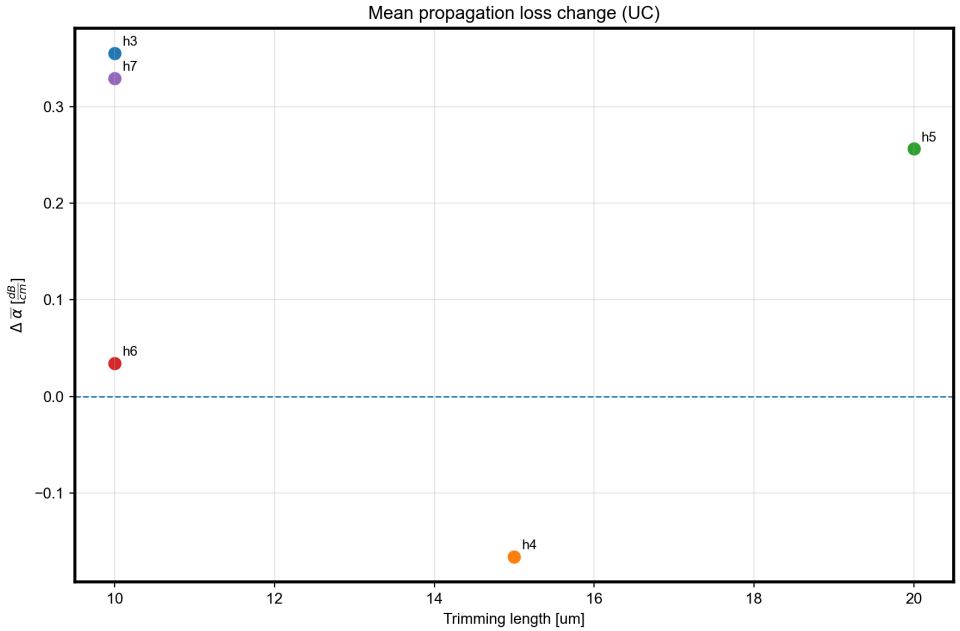


Figure 19: Mean propagation loss change for EBeam devices assuming under coupling.

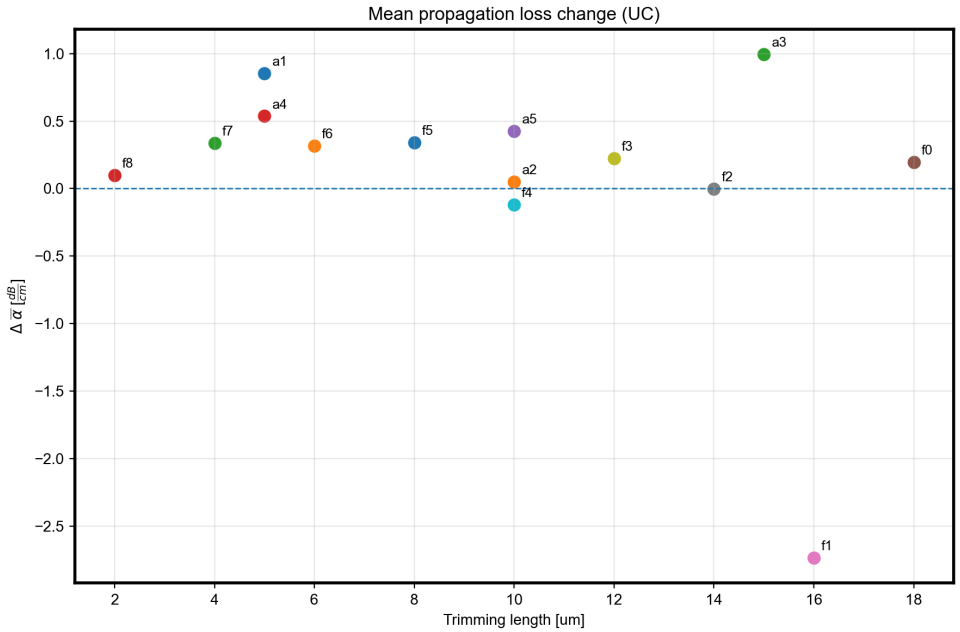


Figure 20: Mean propagation loss change for EBeam devices assuming under coupling.

The calculated propagation losses were again calculated under the assumption of under coupling. It is easily seen, that the EBeam trimmed devices yield maximal propagation loss of $1\frac{dB}{cm}$ with some even showing lowered propagation loss, which is a great improvement compared to FIB trimmed devices.

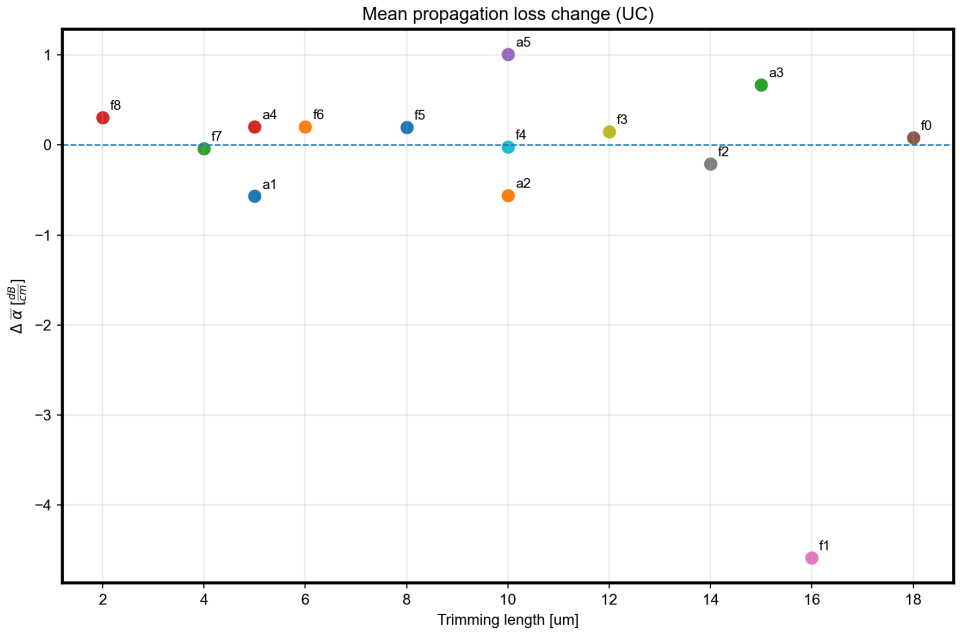


Figure 21: Mean propagation loss change for EBeam devices assuming under coupling and after heat treatment.

Heat treatment shows only small further improvements regarding propagation losses, as

can be seen in Figure 21

Similarly to FIB, there is no clear correlation between trimming length and Q-factor or propagation loss measured. A closer look at resonance peaks for both FIB and EBeam recipes confirm these findings and show instability.

4.3 Improved experimental methodology

The results in the preceding sections demonstrate that the optical response of LNOI devices depends not only on the trimming process itself, but also critically on the measurement conditions. Lithium niobate is substantially more sensitive than silicon nitride to environmental and instrumental variations like temperature, humidity, laser wavelength stability, polarization alignment and fiber-to-chip coupling. These can shift resonance wavelengths and modify Q-factors, making it hard to distinguish between observed changes that are caused by trimming or changes that are caused by measurement variability.

To address this, the deposition recipe and measurement procedure were revised for a second LNOI chip, where the EBeam deposition conditions were adjusted by lowering acceleration voltage from 10kV to 2kV and raising probe current from 150pA to 600pA. This combination reduces electron penetration and substrate damage due to lower voltage, while keeping deposition rate practical through higher probe current. For the measurements, three resonators were reserved as untrimmed references and monitored throughout the measurements and only two resonators were trimmed with the updated recipe.

Over almost two weeks, both reference and trimmed devices were measured multiple times. By evaluating the reference resonators along with the trimmed ones, short term and day-to-day measurement drift could be distinguished from changes caused by carbon deposition. This approach produced trends, as seen in Figure 22, that were significantly clearer and more repeatable than those obtained in the first set of experiments.

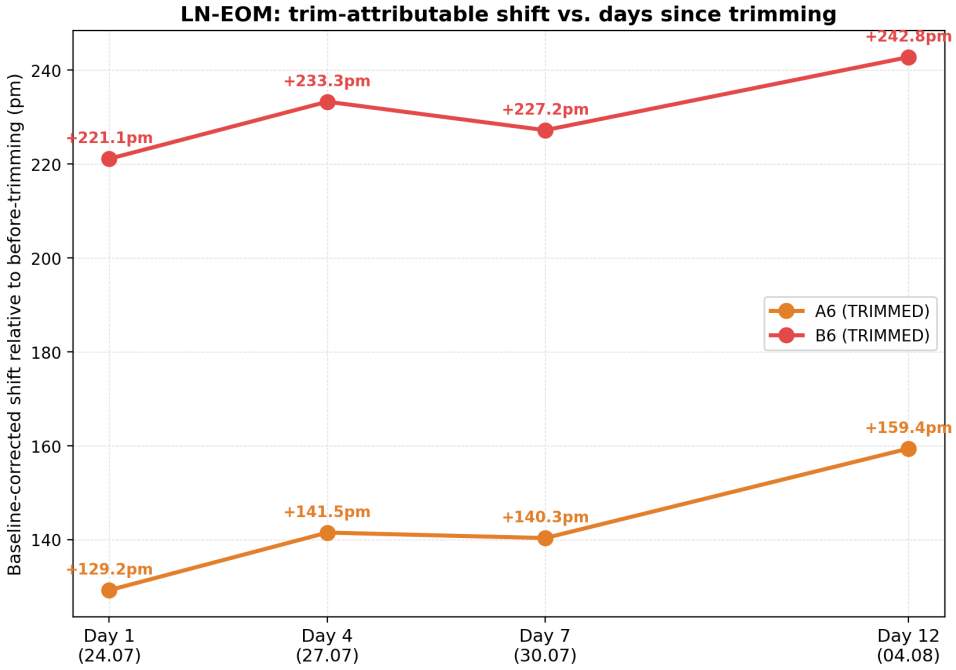


Figure 22: Resonance peak shift stability over two weeks with improved EBeam deposition recipe.

The device A6 has in total $40\mu m$ of deposited carbon composed of four patches with $10\mu m$ length respectively. B6 has in total $60\mu m$ of deposited carbon composed of six patches with again $10\mu m$ length respectively. For A6 a peak shift of $129.2pm$ is measured after trimming, which stays mostly stable, increasing to $159.4pm$ over the two week measurement period. Similar results are reported for B6 with an initial peak shift of $221.1pm$ after trimming, which increases to $242.8pm$ over the two week period.

Contrary to what was seen for FIB, low acceleration voltage and high probe current seem to yield better results for EBeam assisted carbon deposition on LNOI than high voltage and low current. This is probably due to the fact, that electrons do not mill like ions, due to size and mass differences, which causes less to no sputtering by the primary beam. Because of this, higher probe current does not seem to degrade the quality of the waveguide as much as for FIB. Additionally, high voltage with high energy electrons will penetrate much further into the waveguide and substrate, which creates defects like ionization, charging effects or effects where atoms in the lattice are moved by being hit with an electron. Low voltage reduces this penetration depth of electrons and therefore also reduces the volume of substrate and, more importantly, volume of waveguide affected by the primary beam.

Because of this, conditions for viable EBeam deposition seem to be low acceleration voltage and sufficiently high probe current for practical deposition rate, moderate deposition thickness and using a measurement strategy with untrimmed reference resonators mon-

itored over time to distinguish between effects caused by deposition and drift due to environmental and instrumental changes.

4.4 Comparison to results for LTOI

The proposed EBeam method for carbon deposition was used by the group in which this thesis was carried out to trim Lithium tantalate on insulator (LTOI) waveguides. It was possible to report nice linear correlation between resonance peak shift and trimming length in Figure 23.

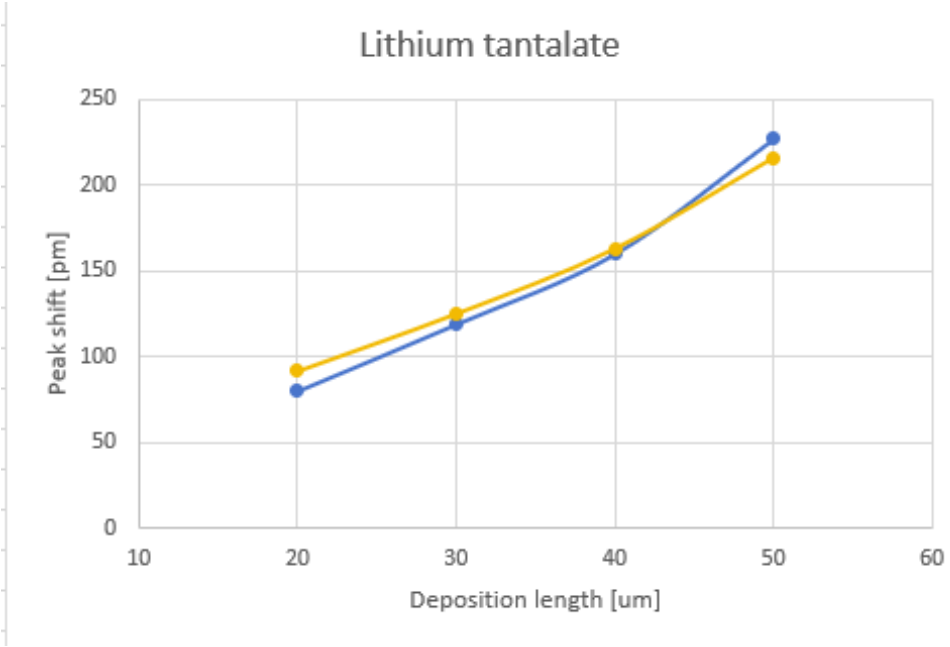


Figure 23: Linear dependence of resonance peak shift and deposition length for LTOI waveguides. The blue line are measurements taken after trimming and the yellow line are measurements taken after trimming and heat treatment at $400°C$ for 20 minutes on a regular hot plate.

In this Figure, the yellow line was measured after heat treating the sample and the blue line right after trimming before heat treatment. Both lines show a lot more stability than what was measured for LNOI.

5 Conclusion

In this section, the primary research question, that will be revisited, is the viability of carbon trimming for LNOI and the emerging LTOI platforms and how this can be improved based on the findings of this work.

5.1 Summary

Different deposition recipes for FIB and EBeam assisted carbon deposition on LNOI waveguides were explored in this thesis. Resonators trimmed with high voltage, low current (30kV, 20pA) FIB recipes with varying trimming lengths and deposition thicknesses showed consistently Q-factor reduction after trimming. The smallest reduction was around 30% and larger reductions ($\approx 48-79\%$) showed for other devices, indicating strong sensitivity to this type of deposition. Devices with lower voltage and high current (5kV, 200pA) FIB recipes showed even bigger Q-factor reduction ($\approx 79\%$ for $<$200nm thickness and $\approx 89\%$ for $<$400nm thickness), implicating that higher probe current causes more damage to the waveguide than higher acceleration voltage. Changes in propagation losses derived from the Q-factors, assuming under coupling, reached very high values up to $\approx 52\frac{dB}{cm}$ for FIB recipes. Higher probe current here also increases loss, which is attributed to greater gallium ion implantation, defect formation and surface sputtering or milling. These degrade the waveguide quality more severely than the deeper but lesser damage from high voltage and low current beams.

EBeam assisted carbon deposition (10kV, 150pA) produced much smaller Q-factor reductions. For that, devices trimmed twice to an estimated thickness of 100nm showed $\approx 5.5-13\%$ reduction and devices trimmed once to 50nm thickness generally showed $\approx 2.5-7.5\%$ reduction, but some devices also show higher reduction up to 22.5%. These values are dramatically better than FIB results and indicate EBeam as the more viable trimming method for LNOI. A post trim heat treatment at 200 $°C$ for 30 minutes improved performance of the EBeam trimmed devices further, where most devices showed Q-factor changes close to zero or slight improvement with one even improving by up to $\approx 50\%$ relative to the untrimmed Q-factor. Propagation loss changes induced by EBeam deposition were generally $< 1\frac{dB}{cm}$, with some even showing reduced propagation loss but heat treatment only provided modest additional improvement.

Despite varying trimming lengths for both FIB and EBeam recipes in the first experiments, no clear correlation between trimming length and either Q-factor or propagation loss was observed, suggesting that process induced damage and measurement variability dominate over length effects in these experiments. Both techniques also showed instability regarding the measured spectra.

That showed that LNOI devices are highly sensitive to environmental and instrumental conditions like temperature, humidity, wavelength stability, polarization and fiber coupling. Recognizing that, the measurement protocol was revised to include untrimmed reference resonators monitored over nearly two weeks alongside trimmed devices. This enabled separation of short term and day-to-day drift from true trimming- induced changes

and yielded clearer, more repeatable trends. The EBeam recipe was adjusted to acceleration voltage of 2kV and probe current of 600pA, which was beneficial for EBeam on LNOI because higher current mainly increases deposition rate without severe waveguide damage due to electrons not sputtering as severely as ions. Lower voltages also reduce penetration depth and limits defect generation in the waveguide and substrate. Using this approach, devices with $40\mu m$ and $60\mu m$ total deposition lengths (in $10\mu m$ patches) showed more stable behaviour with a measured resonance peak shift after trimming of $129.2pm$ and $221.1pm$, respectively.

Applying the same EBeam carbon deposition method to LTOI waveguides produced linear correlation between resonance peak shift and trimming length, both before and after heat treatment. LTOI results were markedly more stable than those for LNOI, indicating that material differences like sensitivity to charge, defects and environmental drift strongly influence trimming reproducibility and optical response.

5.2 Outlook

Concluding the results, Carbon deposition for LNOI seems feasible, but only under carefully chosen conditions with measurement protocol that controls environmental and instrumental drift. EBeam deposition can be clearly viable and promising, but FIB assisted carbon deposition causes large, often unacceptable degradation of resonator performance on LNOI. Current performance limitations are material sensitivity of LNOI, process induced defects, a lack of clear trimming length dependence for certain resonator values and uncertainty regarding actual deposition geometry like thickness due to missing cross section analysis.

Interesting further investigations could include more systematic EBeam parameter sweeps, where acceleration voltage and probe current are varied and an optimal window that minimizes defect generation with good deposition rate is identified. The approach with reference resonators to account for environmental changes could be extended by active environmental control for example through a heated platform, humidity control with strictly defined polarization and improved coupling alignment protocols. Further comparison with LTOI or other platforms under identical trimming conditions is also an interesting approach. LTOI could also be used as a benchmark to identify which LNOI specific mechanisms and properties most limit trimming quality and stability.

6 References

6.1 Acknowledgement

I would like to express my gratitude to Prof. Wolfram Pernice for giving me the opportunity to carry out my thesis in his research group Neuromorphic Quantumphotonics at the Kirchhoff Institute for Physics and I would also like to thank Prof. Katharina Ollefs for agreeing to be the second examiner for this thesis. I am also thankful for all members of the research group, who helped me during measurements in the lab, who gave me the opportunity to get to know more research branches in integrated photonics or who just gave me a warm welcome into the group.

Special thanks go to Dr. Shabnam Taheriniya, who supervised this thesis and was a great help along every step of finalising this thesis, and Vincent Spreter, who helped me during measurements and developing the python script for evaluation.

Erklärung

Ich versichere, dass ich diese Arbeit selbstständig verfasst und keine anderen als die angegebenen Quellen und Hilfsmittel benutzt habe. ChatGPT und Perplexity AI wurden zur Überprüfung der englischen Rechtschreibung, zum Finden von Referenzen und für manche Teile des Python Skripts zur Auswertung verwendet.

Heidelberg, den 07.08.2026,



Nils Anthon

References

[1] D. Zhu, L. Shao, M. Yu, R. Cheng, B. Desiatov, C. J. Xin, Y. Hu, J. Holzgrafe, S. Ghosh, A. Shams-Ansari, E. Puma, N. Sinclair, C. Reimer, M. Zhang, and M. Lončar, "Integrated photonics on thin-film lithium niobate," *Adv. Opt. Photon.* **13**, pp. 242–352, Jun 2021.

[2] G. Chen, N. Li, J. D. Ng, H.-L. Lin, Y. Zhou, Y. H. Fu, L. Y. T. Lee, Y. Yu, A.-Q. Liu, and A. J. Danner, "Advances in lithium niobate photonics: development status and perspectives," *Advanced Photonics* **4**(3), p. 034003, 2022.

[3] R. Xu, Z. Tang, L. McRae, A. Varri, F. Brückerhoff-Plückelmann, X. Ma, J. R. Bankwitz, J. Römer, R. Pradip, Q. Zhang, L. Meyer, Z. Zhao, J. Dijkstra, H. Bhaskaran, R. R. Schröder, W. H. P. Pernice, and S. Taheriniya, "Localized carbon deposition enables trimming of photonic integrated circuits," *Nature Communications* , 2026. Accepted for publication.

[4] R. Xu, S. Taheriniya, A. Varri, M. Ulanov, I. Konyshev, L. Krämer, L. McRae, F. L. Ebert, J. R. Bankwitz, X. Ma, S. Ferrari, H. Bhaskaran, and W. H. P. Pernice, "Mode conversion trimming in asymmetric directional couplers enabled by silicon ion implantation," *Nano Letters* **24**(35), pp. 10813–10819, 2024. PMID: 39164007.

[5] M. Sumets, "Lithium niobate thin films: potential applications, synthesis methods, structure, and properties," in *Lithium Niobate-Based Heterostructures (Second Edition), 2053-2563*, pp. 1–1 to 1–52, IOP Publishing, 2024.

[6] R. Yang, H. Wei, G. Tang, B. Cao, and K. Chen, "Advanced crystallization methods for thin-film lithium niobate and its device applications," *Materials* **18**(5), 2025.

[7] Z. Li, R. N. Wang, G. Lihachev, J. Zhang, Z. Tan, M. Churaev, N. Kuznetsov, A. Siddharth, M. J. Bereyhi, J. Riemensberger, and T. J. Kippenberg, "High density lithium niobate photonic integrated circuits," *Nature Communications* **14**, p. 4856, Aug 2023.

[8] U. Schlarb and K. Betzler, "Refractive indices of lithium niobate as a function of wavelength and composition," *Journal of Applied Physics* **73**, pp. 3472–3476, 04 1993.

[9] Y. Qi and Y. Li, "Integrated lithium niobate photonics," *Nanophotonics* **9**(6), pp. 1287–1320, 2020.

[10] M. Hammer, S. S. Khan, B. Taheri, H. Farheen, and J. Förstner, "Tfln channel waveguides of rib and strip type: properties of guided modes," *Opt. Continuum* **4**, pp. 2356–2385, Oct 2025.

[11] M. Parfenov, P. Agruzov, A. Tronev, I. Ilichev, A. Usikova, Y. Zadiranov, and A. Shamrai, "Metal electrodes for filtering the localized fundamental mode of a ridge optical waveguide on a thin lithium niobate nanofilm," *Nanomaterials* **13**(20), 2023.

[12] R. Wu, M. Wang, J. Xu, J. Qi, W. Chu, Z. Fang, J. Zhang, J. Zhou, L. Qiao, Z. Chai, J. Lin, and Y. Cheng, "Low-loss lithium niobate on insulator (lnoi) waveguides of a 10 cm-length and a sub-nanometer surface roughness," 2018.

[13] E. Jung, X. Ma, J. Brandes, C. Ünlüer, S. Taheriniya, S. Jo, P. Schmidt, E. Biedert, L. McRae, J. R. Bankwitz, F. Brückerhoff-Plückelmann, and W. Pernice, "Octave bandwidth 3D-Printed Couplers for Low-Loss Thin-Film Lithium Tantalate Circuits," 6 2026.

[14] J. R. Bankwitz, J. Dijkstra, R. Pradip, L. McRae, E. Lomonte, F. Lenzini, and W. H. P. Pernice, "Towards “smart transceivers” in fpga-controlled lithium-niobate-on-insulator integrated circuits for edge computing applications

invited

," *Opt. Mater. Express* **13**, pp. 3667–3676, Dec 2023.

[15] M. Hammer, H. Farheen, and J. Förstner, "Guided modes of thin-film lithium niobate slabs," *Opt. Continuum* **3**, pp. 2024–2043, Nov 2024.

[16] K. Okamoto, *Wave theory of optical waveguides*, pp. 1–12. 12 2006.

[17] J. P. Höpker, T. Gerrits, A. Lita, S. Krapick, H. Herrmann, R. Ricken, V. Quiring, R. Mirin, S. W. Nam, C. Silberhorn, and T. J. Bartley, "Integrated transition edge sensors on titanium in-diffused lithium niobate waveguides," *APL Photonics* **4**, p. 056103, May 2019.

[18] N. A. Harper, E. Y. Hwang, P. A. Kocheril, T. K. Lam, and S. K. Cushing, "Subtleties of nanophotonic lithium niobate waveguides for on-chip evanescent wave sensing," *Optics Express* **32**, p. 27931, July 2024.

[19] H. Desmet, W. Bogaerts, A. Adamski, J. Beeckman, K. Neyts, and R. Baets, "Silicon-on-insulator optical waveguides with liquid crystal cladding for switching and tuning," 01 2003.

[20] J. Zhou, W. Hao, and R. Wang, "Adiabatic perturbation theory for mode analysis in optical waveguides with large index variations without eigen value decomposition," *Opt. Express* **33**, pp. 15931–15944, Apr 2025.

[21] M. Hammer, "Metric: Single mode perturbations." `https://metric.computational-photonics.eu/perturb.html`, 2025. Accessed: 4 August 2026.

[22] D. Moskalev, A. Kozlov, U. Salgaeva, V. Krishtop, and A. Volyntsev, "Applicability of the effective index method for the simulation of x-cut linbo3 waveguides," *Applied Sciences* **13**(11), 2023.

[23] M. Huth, F. Porrati, and O. Dobrovolskiy, "Focused electron beam induced deposition meets materials science," *Microelectronic Engineering* **185-186**, p. 9–28, Jan. 2018.

[24] M. Huth, F. Porrati, C. Schwalb, M. Winhold, R. Sachser, M. Dukic, J. Adams, and G. Fantner, "Focused electron beam induced deposition: A perspective," *Beilstein Journal of Nanotechnology* **3**, pp. 597–619, 2012.